A Numerical Study about the Effect of Non-uniform CMAS Penetration on the TGO Growth and Interface Stress Behavior of APS TBCs

Zhenwei CAI
Shanghai Jiao Tong University School of Mechanical Engineering
Zifan ZHANG
Shanghai Jiao Tong University School of Mechanical Engineering
Yingzheng Liu
Shanghai Jiao Tong University School of Mechanical Engineering
Xiaofeng Zhao
Shanghai Jiao Tong University
Weizhe Wang (wangwz0214@sjtu.edu.cn)
Shanghai Jiao Tong University School of Mechanical Engineering

Original Article

Keywords: CMAS non-uniform penetration, TGO growth, Interface stress, Interface roughness

Posted Date: January 9th, 2021

DOI: https://doi.org/10.21203/rs.3.rs-141380/v1

Version of Record: A version of this preprint was published at Chinese Journal of Mechanical Engineering on December 1st, 2021. See the published version at https://doi.org/10.1186/s10033-021-00654-4.

Title page

A numerical study about the effect of non-uniform CMAS penetration on the TGO growth and interface stress behavior of APS TBCs

Zhen-Wei Cai, born in 1992, is a postdoctor at *Key Laboratory of Power Machinery and Engineering, School of Mechanical Engineering, Shanghai Jiao Tong University, Shanghai 200240, China*. His main research direction is the strength evaluation of high-temperature structural components and the intelligent manufacturing of advanced thermal barrier coatings
Tel: +86-18801733509; E-mail: xiaoyezhu1992@sjtu.edu.cn

Zi-Fan Zhang, born in 1996, is currently a master student at *Key Laboratory of Power Machinery and Engineering, School of Mechanical Engineering, Shanghai Jiao Tong University*. His main research direction is the strength evaluation of thermal barrier coatings.
E-mail: 954143356@sjtu.edu.cn

Ying-Zheng Liu, born in 1972, is currently a professor at *Key Laboratory of Power Machinery and Engineering, School of Mechanical Engineering, Shanghai Jiao Tong University, Shanghai 200240, China.* He is the director of *Gas Turbine Research Institute, Shanghai Jiao Tong University, Shanghai 200240, China*
E-mail: yzliu@sjtu.edu.cn

Xiao-Feng Zhao, is currently a professor at *School of Materials Science and Engineering, Shanghai Jiao Tong University, Shanghai 200240, China.* His main research direction is high-temperature coatings, such as thermal barrier coatings used in aero engines and gas turbines, anti-corrosion coatings for nuclear reactor fuel claddings, and other anti-oxidation and wear-resistant coatings.
E-mail: xiaofengzhao@sjtu.edu.cn

Wei-Zhe Wang, born in 1977, is currently a professor at *Gas Turbine Research Institute, Shanghai Jiao Tong University, Shanghai 200240, China.* He mainly focuses on the major national demand industries (aviation, ground gas turbines, smart energy), and conducts research on digital twin technology of process systems and component systems.
Tel: +86- 021-34205083; E-mail: wangwz0214@sjtu.edu.cn

Corresponding author：Wei-Zhe WANG　E-mail：wangwz0214@sjtu.edu.cn

ORIGINAL ARTICLE(or REVIEW)

A numerical study about the effect of non-uniform CMAS penetration on the TGO growth and interface stress behavior of APS TBCs

Zhen-Wei Cai[1, 2] • Zi-Fan Zhang [1, 2] • Ying-Zheng Liu [1, 2] • Xiao-Feng Zhao [3] • Wei-Zhe Wang [1,2]

Received June xx, 201x; revised February xx, 201x; accepted March xx, 201x

Abstract: The penetration of CaO-MgO-Al_2O_3-SiO_2 (CMAS) (CMAS) is one of the most vital factors inducing the failure of air plasma sprayed thermal barrier coatings (APS TBCs). The CMAS penetration into the porous microstructures of TBCs changes the thermal/mechanical properties of top coat (TC) material, this brings about considerable thermal mismatch stress at the TC/bond coat (BC) interface, and accelerates the growth of the thermally grown oxide (TGO), finally leading to more complicated stress state at the interface. In present study, a two-dimensional global model of APS TBCs with half of the TC penetrated by CMAS is built to study effect of non-uniform CMAS penetration. Then, a local model extracted from the global are built to investigate the effect of interface morphologies and CMAS penetration depth. The results showed that non-uniform CMAS penetration in APS TBCs causes non-uniform TGO growth, which further leads to more complicated interface stress distribution. The CMAS penetration depth had a greater effect on the TC/TGO interface stress behavior, while the interface roughness had an more obvious influence on the stress level at BC/TGO interface under CMAS penetration.

Keywords: CMAS non-uniform penetration • TGO growth • Interface stress • Interface roughness

✉ Wei-Zhe WANG
wangwz0214@sjtu.edu.cn

[1] Key Laboratory of Power Machinery and Engineering, School of Mechanical Engineering, Shanghai Jiao Tong University, Shanghai 200240, China

[2] Gas Turbine Research Institute, Shanghai Jiao Tong University, Shanghai 200240, China

[3] School of Materials Science and Engineering, Shanghai Jiao Tong University, Shanghai 200240, China

1 Introduction

Air plasma sprayed thermal barrier coatings (APS TBCs) are widely used in gas turbines as a critical thermal insulation component [1]. Nowadays, the penetration of environmental CaO-MgO-Al_2O_3-SiO_2 (CMAS) is one of the most vital factors inducing the failure of APS TBCs [2-4]. The penetration of CMAS into the porous microstructures of the ceramic top coat (TC) of APS TBCs can cause substantial surface modification of this layer. Firstly, CMAS-penetration induced change of the mechanical parameters of TBCs brings about considerable thermal mismatch stress at the TC/metallic bond coat (BC) interface. Secondly, CMAS penetration-induced thermal parameter change also weakens the thermal insulation ability of TBCs, which furtherly accelerates the growth of the thermally grown oxide (TGO), and this finally leads to a more serious stress state at the TC/BC interface or even the premature initiation of the interface cracks [5]. Thus, understanding the CMAS penetration effect on the TGO growth and interface stress behavior of APS TBCs is of great value.

Many researchers have focused on the CMAS-penetration induced surface modification of TBCs experimentally or theoretically. Due to the considerable difference of the material properties between CMAS and TC material, CMAS infiltrated TC layer displays totally different thermal/mechanical behavior than that without CMAS penetration [6]. Siddharth et al. [7] applied micro-hardness measurement to obtain the mechanical properties in APS TBCs after CMAS penetration, and found an obvious improvement of Young's modulus together with a decrease of the shrinkage of TBCs. Kakuda

et al. [8] found that the penetration of CMAS leads to approximately two-fold increase of thermal conductivity of TBCs, and this would further cause an increase of the temperature at TC/BC interface, accelerating the growth of TGO or even the premature spallation of TBCs (shown in Figure 1 (a)) [2, 9-10]. However, the microstructure distribution or the porosity in APS TBCs mainly depends on the spraying process, this results that the experimentally measured material properties change of CMAS penetrated APS TBCs varies in different samples. Therefore, many studies applied simplified theoretical models to consider the effect of CMAS penetration on the thermal/mechanical properties of TBCs, and shows a highly agreement with the experimental results [11-15]. To conclude, both the thermal/mechanical change of TBCs induced by CMAS penetration have a significant effect on the thermal/mechanical properties of the TBCs. Some experiments also noticed that a premature spalling from the interface occurred in the APS TBCs with CMAS penetration, as is shown in Figure 1(b) [5]. However, the mechanism of CMAS-penetration induced interface cracking behavior in the APS TBCs is still poorly understood. In this respect, some numerical studies have been carried out to investigate the CMAS penetration effect on the stress behavior at TC/BC interface. Zhang et al. [16] found that the CMAS penetration depth has an influence on the interface stress behavior of TBCs because that the depth of CMAS penetration determines the modified area in TBCS, but this study did not consider the effect of the interface roughness and TGO growth, which is one of most factors inducing the interface cracks [17-19]. Su et al. [13] found that the increases of the Young's modulus of TC layer induced CMAS penetration accelerated the initiation and propagation of cracks on the rough interface of TBCs, but ignored the effect of thermal properties change of TBCs. In addition, the peeling of TBCs caused by CMAS penetration often occurs in local areas [5, 20], which might be owing to the non-uniform distribution of CMAS deposits on the TBCs surface (shown in Figure 1(c), causing the non-uniform CMAS penetration at different areas in TBCs. However, there are few published results on the effect of CMAS non-uniform penetration on the TGO growth and interface stress behavior. To better understand this effect, it is important to carry out some researches about the CMAS penetration effect on the TGO growth and interface stress behavior of APS TBCs.

This study numerically investigated the influence of CMAS penetration on the TGO growth and stress behavior at the TC/BC interface. A two-dimensional global model of APS TBCs with half of the TC penetrated by CMAS is firstly built to study effect of non-uniform CMAS penetration. In this model, the temperature gradient in APS TBCs and the dynamic TGO growth is considered. The change of thermal/mechanical properties induced by CMAS penetration is appropriately considered by some theoretical models. A local model extracted from the global are built to investigate the effect of interface morphologies and CMAS penetration depth. To simplify the irregular interface morphology in TBCs, the morphology was assumed to be a perfect sinusoid.

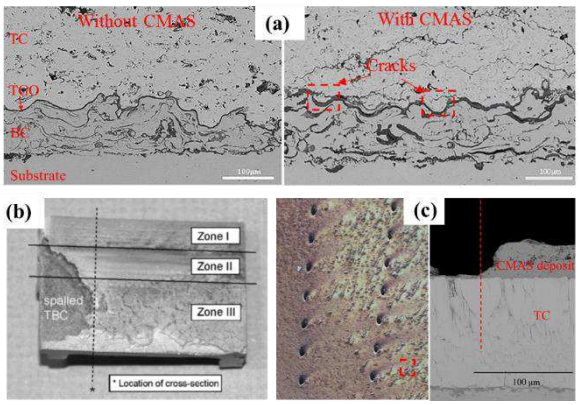

Figure 1 (a) Cross-section of APS TBCs without/with CMAS penetration; (b) Cross-section image of the uniform CMAS deposit distribution around the dividing line; (c) Plan view optical image of a segment of a turbine shroud.

2 Numerical model

2.1 Theoretical Basis of the surface modification

The CMAS penetrated TC layer could be regarded as a two-phase composite material. Thus, effective medium theory can be used for the evaluation of the thermal/mechanical properties of TBCs after CMAS penetration, and calculation results would be compared with the experimental results from the literatures. Before applying the theory, several assumptions are made: ① The CMAS deposit is enough to completely fill each pore in TC layer; ② The reaction effects between TC material and CMAS are not considered, thus the phase transformation of TC material during the cooling stage is ignorable; ③ The TC materials are isotropic before and after CMAS infiltration.

Young's modulus

The mechanical properties of two-phase composite material depend on the concentration, shape, continuity and the spatial distribution of each phase [21]. The TC

layer infiltrated by CMAS can be regarded as a composite material mixed with CMAS and TC materials. At present, there are two widely used models (Voigt model and Reuss model) to describe the mechanical properties of composite material containing two elastic isotropic components [22-23]. Among them, the Voigt model assumes that the load causes equal strain in the two phases, and the stress of the composite material is the sum of the stresses afforded by each phase. Therefore, the Young's modulus of the ceramic layer penetrated by CMAS can be written as the weighted average Young's modulus of each phase's volume fraction:

$$E_f = E_c V_c + E_t V_t, \quad (1)$$

Where the subscript *c* represents CMAS, *t* represents the TC material, and *f* represents the material parameters of the TC layer after CMAS infiltration. E_c And E_t are the Young's modulus of CMAS and TC material (bulk), respectively, V_c and V_t are the volume fractions of CMAS and TC layer, respectively. Generally, the porosity of the ceramic layer is 10%, thus there is V_c = 0.1, V_t = 0.9.

The Reuss model assumes that the stress in the two phases in the composite are equal, thus the total strain of the composite is equal to the sum of the strains in each phase. Therefore, the Young's modulus of the TC layer penetrated by CMAS can be described as:

$$E_f = (\frac{V_c}{E_c} + \frac{V_t}{E_t})^{-1}, \quad (2)$$

Comparing the results calculated from the above two models with the experimental results, it could be found that Reuss model has a higher accuracy [21, 24]. Therefore, the present study will use Reuss model to calculate the Young's modulus of CMAS penetrated TC layer. In addition, it is generally believed that CMAS penetration almost has no effect on the Poisson's ratio of TC material [21].

Thermal expansion coefficient

The thermal expansion coefficient of TC layer after CMAS penetration can be described by Schapery model [25]:

$$\alpha_f = \frac{\alpha_c E_c V_c + \alpha_t E_t V_t}{E_c V_c + E_t V_t}, \quad (3)$$

Where α_c and α_t are the thermal expansion coefficients of CMAS and TC material, respectively. It can be seen that the thermal expansion coefficient of TC layer after CMAS penetration has an obvious relationship with the porosity in TC layer and the thermal expansion coefficient of CMAS. Studies have shown that the penetration of CMAS with different composition leads to a 5%~15% decrease of the thermal expansion coefficient for TBCs with a porosity of 0.1 [21]. In the present study, the thermal expansion coefficient of the TC layer is reduced by 6.2% after CMAS penetration according to Eqs (3), which is in agreement with the range provided in the above literature.

Thermal conductivity

The microstructure characteristics in APS TBCs are extremely complex, and the size, shape and distribution of the microstructures significantly affect the thermal conductivity of coatings. Many studies have analyzed the relationship between the microstructure characteristics thermal conductivity in APS TBCs [24, 26-30]. To conclude, there are two theoretical methods: Maxwell model [14] and Rayleigh model [15], which are widely used to obtain the thermal conductivity of APS TBCs after CMAS penetration. Among them, Maxwell model assumes that the microstructures in TC layer are spherical and do not contact each other, then the thermal conductivity of TC layer penetrated by CMAS is:

$$k_f = k_t \left[1 + 3V_c (\frac{\gamma + 2}{\gamma - 2} - V_c)^{-1} \right], \quad (4)$$

Where k_c and k_t are the thermal conductivity of CMAS and TC material, respectively, $\gamma = k_c / k_t$, is the ratio of the thermal conductivity in CMAS and TC material.

The Rayleigh model can be written as:

$$k_f = k_t \left[1 + V_c (\gamma - 1_c) \right], \quad (5)$$

In Refs [8], the Maxwell model and Rayleigh model are used to calculate that the thermal conductivity of TC layer after CMAS penetration is reduced by 10% and 2%, respectively. This shows that the Rayleigh model has a better calculation accuracy, so the present study will apply the Rayleigh model to calculate the thermal conductivity of CMAS penetrated TC layer.

Specific heat

Generally, the specific heat of TC layer after CMAS penetration is related to the specific heat, volume fraction and density of each phases, and it can be written as:

$$C_f = C_t \omega_t + C_c \omega_c, \quad (6)$$

Where C_t and C_c are the specific heat of the TC material and CMAS, respectively; ω_t and ω_c are the mass fractions of the TC material and CMAS, which can be written as:

$$\omega_i = \frac{V_i \rho_i}{\sum_{j=1}^{2} V_i \rho_i}, \quad (7)$$

Where ρ_i is the density of each phase. The specific heat calculated by Eqs (6) differs by 4% from the experimental results [8], indicating that this model can be used in the calculation of the specific heat of CMAS penetrated TC layer.

Density

Based on the assumption that the phase change of the TC material is not considered in the present study, the density of CMAS penetrated TC layer can be calculated from [8]:

$$\rho_f = V_t \rho_t + V_c \rho_c, \quad (8)$$

It should be noted that the TC material used in the above Eqs is bulk material, which is different from those with the consideration of the microstructures in TC layer.

2.2 FEM model and boundary conditions

Global model

Figure 2(a) shows a two-dimensional multi-period global model of APS TBCs with CMAS non-uniform penetration. The multi-period means that the model is long enough in x axis to consider more interface morphologies. In the model, the thickness of TC layer H_{TC} is 300μm, the thickness of the BC layer H_{BC} is 180μm, the thickness of the substrate H_{SUB} is 3mm, and the initial thickness of the TGO layer H_{TGO} is 1μm. The dynamic growth of TGO is considered in the simulation process. In order to consider the influence of the interface roughness in APS TBCs, the interface morphology in the model is simplified as perfect sinusoid [17-18]. The sinusoidal curve is given as $y(x) = A \cdot \sin(2\pi x/\lambda)$, thus the roughness of the interface is controlled by the amplitude A and the wavelength λ, which are obtained from observation of the cross-sectional morphology in experiments [31]. In this study, λ is set to a constant value of 80 μm, and amplitude A was from 5 μm to 20 μm, as shown in Figure 2(a). According to the size of the CMAS non-uniform coverage area on the blade surface shown in Figure 1(c), the length of the global model L is set to 6.24 mm, which contains 78 sinusoidal periods at the TC/TGO/BC interface. The influence of CMAS penetration is considered by the thermal/mechanical change of TC layer, and previous studies have demonstrated that CMAS had the greatest effect on the interface stress behavior when it penetrates to the bottom of the TC layer [21]. Therefore, in order to investigate the effect of non-uniform CMAS penetration, the left half TC layer in the model is completely penetrated by CMAS, that is, the penetration depth H_{CP}=H_{TC}=300μm, while the right half is not penetrated by CMAS. Considering that the APS TBCs model is assumed as one part from the blade, thus the left and right boundaries of the model should be set as multi-point constraint (MPC) to ensure that all points at the boundaries can simultaneously move in the x direction. The bottom boundary of the model is constrained in the y direction, while the upper surface boundary is a free. The heat flux on the left and right boundary is 0 (adiabatic).

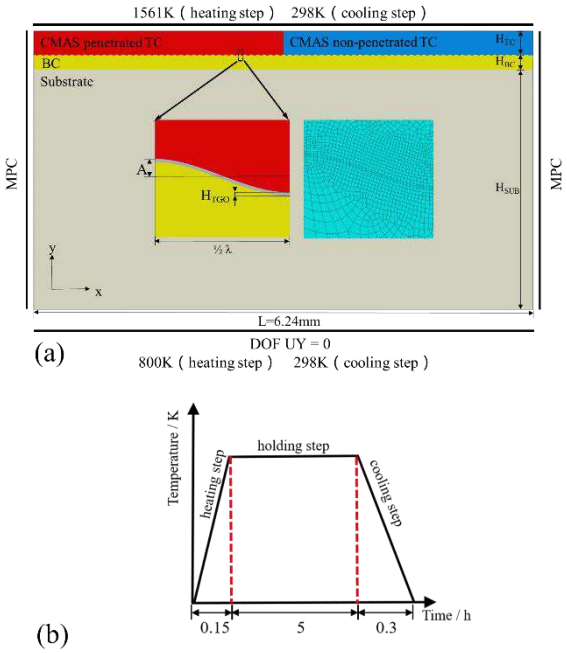

Figure 2 (a) The two-dimensional multi-period global model of APS TBCs with CMAS non-uniform penetration; (B) Thermal boundary conditions of the model.

The element type used in the model is 4-node plane strain thermally coupled quadrilateral, bilinear displacement and temperature (CPE4T). Refined meshes are applied in the zone around TGO layer to improve the stress estimation accuracy here. In order to investigate the influence of CMAS penetration on the temperature distribution in TBCs, a thermal cycle condition is calculated in this study [32]. As is shown in Figure 2(b), the initial temperature of the model is 298K. During the heating process, the temperature at the upper surface rises to 1561K linearly in 0.15h, while the temperature at the lower surface rises to 800K. The dwell time is 5h, then the temperature at the upper and lower surfaces dropped to 298K at the cooling process (0.3h). Finite element analysis was conducted employing the commercial software ABAQUS 6.13 [33].

Local model

In order to further study the influence of CMAS penetration depth and interface roughness on the interface stress behavior in APS TBCs under non-uniform CMAS penetration, a critical zone is selected for locally modeling based on the results from the multi-period global model. As shown in Fig 3a, the critical zone II is located around the dividing line of CMAS in the multi-period model. In order to observe the TGO growth behavior caused by the local non-uniform CMAS penetration around the dividing line, zone II includes two-period length (2*L*): the left period with CMAS penetration, while right one without CMAS penetration, as is shown in Figure3c. The constraints and thermal boundary conditions of the local model is consistent with the multi-period model. The effects of different CMAS penetration depths (H_{CP}=0μm, 100μm, 200μm, 300μm) on the TGO growth and interface stress behavior are studied. The influence of different interface roughness under CMAS penetration is also discussed.

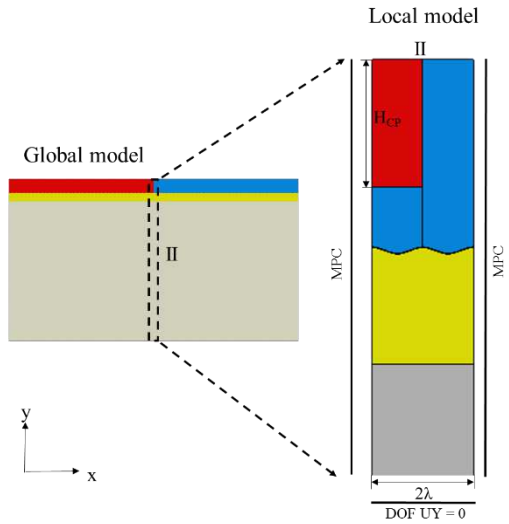

Figure 3 The local model of the critical zone II**.**

Material parameters

In the present study, the TC material is ZrO_2-8wt.% Y_2O_3 (8YSZ), while the material of the BC is NiCoCrAlY, and the material of the substrate is Hastelloy-X. The TC layer is assumed to as visco-elastic material, while other layers are visco-plastic. For APS TBCs without CMAS penetration, the fundamental material properties of each layer are shown in Table 1. The CMAS penetration only changes the material properties of TC layer. As is shown in Table 2, the thermal/mechanical properties of CMAS penetrated TC layer are calculated based on Eqs (1) to (8), and the results are in agreement with the range of the material change in the previous studies [8, 21, 24]. It can be seen from Table 2 that the elastic modulus, equivalent thermal conductivity, and specific heat capacity of TC layer increased after CMAS infiltration, especially the thermal conductivity increased nearly twice; while the equivalent density and the equivalent thermal expansion coefficient reduced. The creep behavior of all of the layers is described by the Norton equation $\dot{\varepsilon}_{cr} = B\sigma^n$,where $\dot{\varepsilon}_{cr}$, σ are the creep strain rate and the stress respectively, and B, n are material properties. The corresponding creep parameters of each layer are listed in Table 3.

Table 1 Material properties for all layers of the APS TBCs [35-39]

	T (°C)	*E* (GPa)	*v*	*α* (/10^6K)	*k* (W/mK)	*C* (J/kgK)	*ρ* (kg/m^3)
TC	25	17.5	0.2	9.68	1.05	483	5650
	800			9.88			
	1000	12.4		10.34			
TGO	25	380	0.27	5.1	25.2	857	3978
	800	338					
	1000	312		9.8			
BC	25	220	0.3	10.3	4.3	501	7320
	400	200		12.7	6.4	592	
	800	164		14.1	10.2	781	
	1000	120		20.4	11.1	764	
SUB	100	209	0.38	11.1	11.4	544	8110
	300	199	0.38	13.3	14.9		
	500	185	0.39	14.0	18.3		
	700	167	0.39	14.6	21.8		
	900	145	0.40	15.4	25.2		
	1100	123	0.40	17.3	28.7		

Table 2 Material properties of CMAS penetrated TC layer [41].

T (°C)	*E* (GPa)	*v*	*α* (/10^6K)	*k* (W/mK)	*C* (J/kgK)	*ρ* (kg/m^3)
25	19	0.2	8.57	2.09	501	5339
1000	12.4		10.34			

Table 3 The creep parameters of different layers in APS TBCs [40].

Layer	B($s^{-1}MPa^{-1}$)	n
TC	$1.8e^{-11}$–$1.8e^{-5}$	1
BC	$2.15e^{-8}$	2.45
SUB	$7.54e^{-28}$	4.78

TGO growth model

The TGO layer will grow at high temperature, its growth rate is related to temperature and time. The thickness of TGO layer could be written as [34]:

$$h_{TGO} = c \cdot \exp(-\frac{Q}{R \cdot T}) t^n , \quad (9)$$

Where, h_{TGO} is the thickness of the TGO layer, R is the universal gas constant, T is the temperature, t is the time, n is the BC layer oxidation exponent, C and Q are fitting parameters. These parameters are shown in Table 4.

The TGO growth process can be approximated as the expansion along thickness direction, and its expansion (growth) strain can be written as:

$$\varepsilon_{\mathrm{TGO}} = \ln \frac{h_{TGO}}{h_0} , \quad (10)$$

Where h_0 is the initial thickness of TGO, which is generally set as 1μm, thus the TGO growth rate could be written as:

$$\dot{\varepsilon}_{\mathrm{TGO}} = \frac{d\varepsilon_{\mathrm{TGO}}}{dt} = \frac{nk_p t^{n-1}}{k_p t^n + h_0} , \quad (11)$$

And there is:

$$\dot{\varepsilon}_{TGO}(0) = 0 , \quad (12)$$

It can be deduced that TGO growth rate $\dot{\varepsilon}_{TGO}$ decreases with time. In ABAQUS software, the TGO growth can be simulated by defining the anisotropic swelling of the material.

3 Results and discussion

3.1 TGO growth and interface stress behavior in APS TBCs under non-uniform CMAS penetration

Figure 4(a) shows the temperature distribution of the multi-period model of APS TBCs under the non-uniform CMAS penetration. It is obvious that the temperature distributions are different at the areas with or without CMAS penetration. In the left half model, CMAS penetration leads to the deterioration of the thermal insulation performance in this area. Therefore, the temperature in the left half model is significantly higher than that on the right half model, this furtherly induces a transverse (x direction) heat flow from left part to the right part in the model. There are temperature gradients both in transverse direction and thickness direction, which is more complicated than the situation without CMAS non-uniform penetration. In order to further study the temperature distribution in different areas of model, three paths along the thickness direction are selected: path 1(the life side of the model), path 2 (the life side of the model), and path 3 ((the right side of the model), as is shown in Fig4a. Fig 4b displays the temperature distortion along the three paths. The temperature gradient of TC layer along path 1 is much smaller than that along path 3, this indicates that CMAS Penetration will have a greater effect on the temperature distribution at the interface. The temperature gradient of TC layer along Path 2 is between the results of Path 1 and Path 3, indicating that the non-uniform CMAS penetration causes a temperature change in transverse direction, which will affect the TGO growth at the interface.

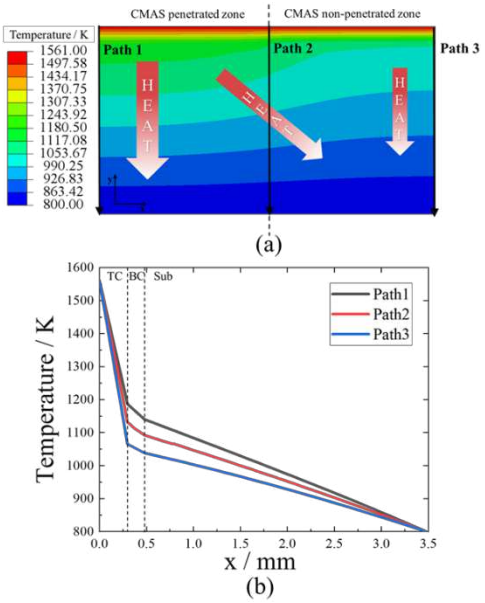

Figure 4 (a) The temperature distribution of the multi-period global model of APS TBCs under the non-uniform CMAS penetration; (b) The temperature distributions along THEthree paths in the model.

To make the analysis clearer, another two critical zone (zone I and zone III) are selected, as is shown in Figure 5(a). Due to the huge length of the multi-period global model, CMAS penetration in zone I is approximately uniform (H_{CP}=300μm), while zone III can be approximately regarded as not being affected by CMAS penetration (H_{CP}=0μm). Figure 5(b) shows the temperature distribution at the interface of the multi-period model after the heating process. It can be clearly noticed that the

temperature at the interface of CMAS penetrated half model is much higher than that of CMAS non penetrated right half model. The maximum temperature difference at the interface from the left side and right side of the model can reach 120K, and the closer to the dividing line, the larger the traverse temperature gradient is. In addition, it can be observed that the temperature distribution displays small fluctuations along the interface, which is caused by the interface roughness. Figure 5(c) shows the interface temperature distribution in three critical zones: I, II, and III. Among them, the interface temperature curve in zone I and zone III are relatively gentle, while transverse temperature difference in zone II can reach 22K, this might cause non-uniform TGO growth in this region. At the same time, the interface roughness also causes the non-uniform TGO growth at the peak and valley locations in one interface period. These effects will cause a more complex TGO growth behavior in zone II, and further has the influence on the interface stress behavior here.

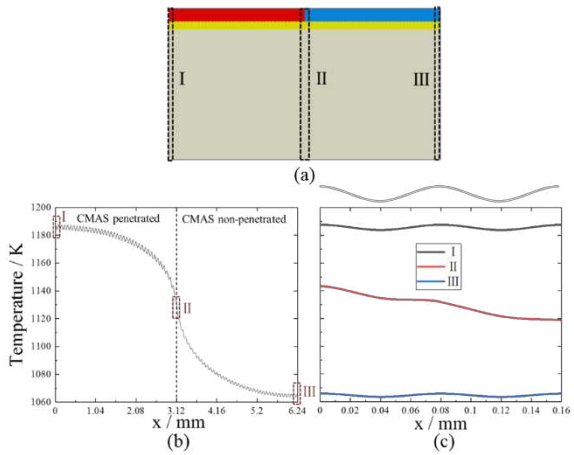

Figure 5 (a) The critical zones: I, II and III; (b) the temperature distribution at the interface of the multi-period model after the heating process; (c) the interface temperature distribution in three critical zones: I, II, and III.

Figure 6(a) illustrates the distribution of TGO thickness in the multi-period global model. Consistent with the temperature distribution shown in Figure 5(a), the TGO thickness in the CMAS penetrated side of APS TBCs can reach 2.18μm, which is significantly higher than that in the non-penetrated side (1.45μm). In addition, as is shown in Figure 6(b), TGO thickness at zone I is also larger than that at zone III, which might further cause the different interface stress behavior in the two regions. Although TGO thickness in zone II is smaller than that in zone I, the transverse temperature difference around the dividing line causes the left side TGO thickness larger than that at the right side. This non-uniform TGO growth behavior around the dividing line of CMAS will further affect the interface stress behavior here, which will be discussed next.

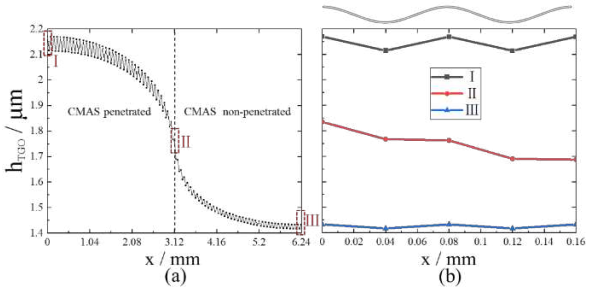

Figure 6 (a)The distribution of TGO thickness in the multi-period global model of APS TBCs; (b) The distribution of TGO thickness in three critical zones: I, II, and III.

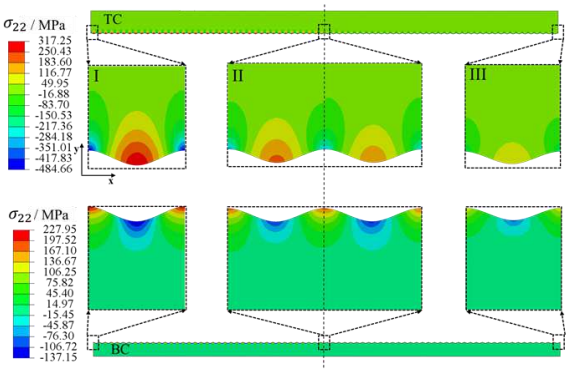

Figure 7 The σ_{22} distribution in TC and BC layer of the multi-period global model of APS TBCs at room temperature

Generally, the initiation of the interface cracks mainly depends on the interface tensile stress at thickness direction (y-axis) σ_{22}, and σ_{22} increases gradually and reaches its maximum at the end of the cooling process. Therefore, only σ_{22} at the end of the cooling process was obtained and analyzed in this study. Figure 7 shows the σ_{22} distribution in TC and BC layer of the multi-period global model of APS TBCs at room temperature. As is shown in this figure, σ_{22} concentrated in the valley locations around the interface of TC layer, while stress state at the peak positions is compressive. Comparing the stress distribution in the three critical zones of TC layer, it is found that σ_{22} is proportional to TGO thickness there (shown in Figure 6 (b)), thus σ_{22} at zone I is the largest, followed by that at zone II, and σ_{22} at zone III is the smallest. Among them, the maximum σ_{22} in zone I can reach 317 MPa, and the maximum σ_{22} in the zone III is 110 MPa. The non-uniform TGO growth around dividing line in region II leads to a stress difference between the left and right sides, and the maximum stress difference can reach 40 MPa. Contrary to the stress distribution in TC layer, σ_{22} in the BC layer mainly concentrated at the peak locations around the interface, while stress state at the

valley locations is compressive. The stress level in BC layer is a little small compared to that in TC layer, and the stress difference between the left and right sides in zone II also exists in BC layer. Above results indicate that the non-uniform CMAS penetration in APS TBCs will result in non-uniform interface stress distribution at the interface, and tensile stress σ_{22} at the interface of CMAS penetrated area is much larger than that in the non-penetrated area.

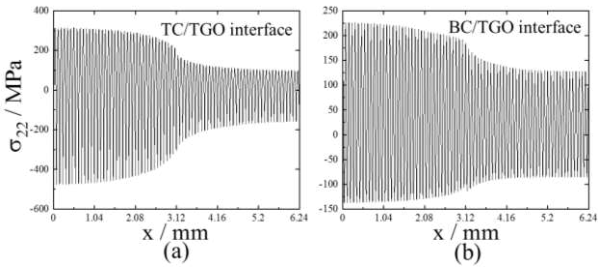

Figure 8 The σ_{22} distribution at (a) TC/TGO and (b) BC/TGO interface of the multi-period global model of APS TBCs

Figure 8 further shows the σ_{22} distribution at the TC/TGO and BC/TGO interface of the multi-period global model of APS TBCs under non-uniform CMAS penetration. The different stress state at the peaks or valleys in one-period interface demonstrates that the interface roughness has a great influence on the interface stress distribution. Furthermore, the stress difference between the peak and valley in the left side interface is much larger than that of the right side interface, indicating that CMAS penetration aggravates the stress difference induced by the interface roughness. In addition, it can be observed that the degree of CMAS penetration effect on the stress level at TC/TGO and BC/TGO interface is different. Figure 9 further shows the σ_{22} distribution at the interface in the three critical zones. As shown in Figure 9(a), σ_{22} at the valleys of the TC/TGO interface increases from 98 MPa (zone III) to 317 MPa (zone I) CMAS penetration. In zone II, an obvious stress difference occurs at the two peak locations around dividing line. As shown in Figure 9(b), the stress state at the BC/TGO interface is opposite to that at the TC/TGO interface. σ_{22} at the of peaks the BC/TGO interface increases from 125 MPa (zone III) to 228 MPa (zone I). Comparing the stress distribution at the two interfaces, it can be found that CMAS penetration has a greater effect on the σ_{22} at TC/TGO interface. To conclude, for the TC/TGO interface, CMAS penetration might accelerate the cracks initiation at the valleys; for the BC/TGO interface, CMAS penetration might accelerate cracks initiation at the peaks.

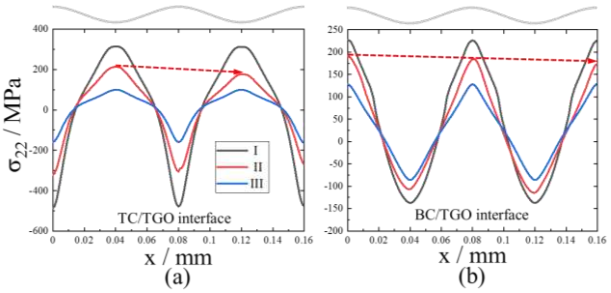

Figure 9 The σ_{22} distribution at (a) TC/TGO and (b) BC/TGO of the three critical zones.

3.2 The effect of CMAS penetration depth

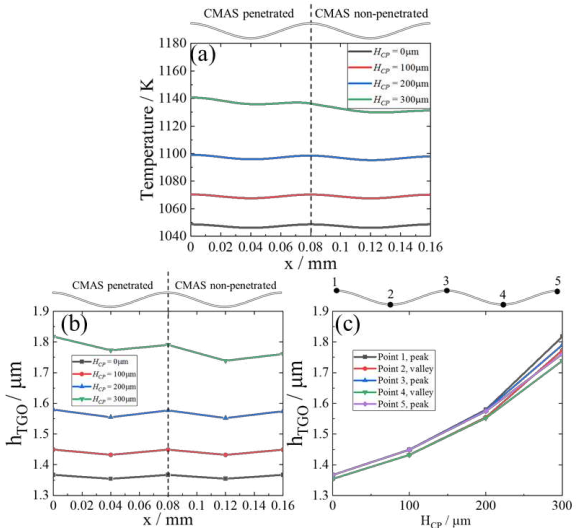

Figure 10 (a) The temperature distribution at the interface of zone II under different CMAS penetration depths (H_{CP}=0μm, 100μm, 200μm, 300μm); (b) the distribution of TGO thickness under different CMAS penetration depths; (c) TGO thickness at the peaks and valleys of the interface under different CMAS penetration depth

Figure 10(a) shows the temperature distribution at the interface of zone II under different CMAS penetration depths (H_{CP}=0μm, 100μm, 200μm, 300μm). The results are calculated based on the local model of zone II (shown in Figure 3). The interface temperature distribution on the two sides of the interface is completely symmetrical without CMAS penetration (H_{CP}=0μm). As the CMAS penetration depth increases, the interface temperature gradually gets higher, this is due to the thermal conductivity change of the CMAS penetrated part of TC layer. When the left part of TC layer is completely penetrated by CMAS (H_{CP}=300μm), the temperature at the left side interface increase by 90K (x=0mm) compared to the results without CMAS penetration. In addition, the temperature difference between the life and right side

around the dividing line becomes larger as CMAS penetration depth increases. To further investigate effect of the temperature difference on the TGO growth behavior, Figure 10(b) shows the distribution of TGO thickness under different CMAS penetration depths. Consistent with the temperature distribution shown in Figure 10(a), the TGO layer gradually gets thicker as CMAS penetration depth increases. Figure 10(c) further exhibits TGO thickness at the peaks and valleys of the interface under different CMAS penetration depth. It can be seen that the difference of TGO thickness between the life and right side around the dividing line increases with CMAS penetration depths. This indicates that CMAS penetration accelerate the non-uniform TGO growth around the dividing line, which might further affect the interface stress behavior here.

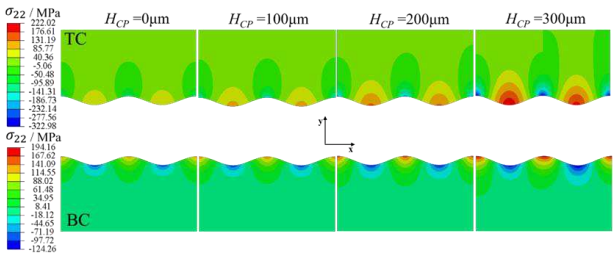

Figure 11 The σ_{22} distribution in TC and BC layer of zone II under different CMAS penetration depths.

Figure 11 exhibits the σ_{22} distribution in TC and BC layer of zone II under different CMAS penetration depths. Similar to the stress distribution at the interface of the multi-period model, the stress difference exists around the dividing line. As CMAS penetration depth increases, the tensile stress both in TC and BC layer increase considerably, and the maximum stress appears at the interface. Figure 12 further displays the σ_{22} distribution at the TC/TGO and BC/TGO interface under different CMAS penetration depths. It can be noticed that when CMAS penetration depth increases, the σ_{22} difference around the dividing line becomes larger. In addition, the influence of CMAS penetration depth on the stress behavior at the two interfaces is also different. When TC layer is completely penetrated by CMAS, the stress difference around the dividing line at the valleys of TC/TGO interface can reach 30MPa, while that at the peaks of BC/TGO interface is almost equal to 0 MPa. This demonstrates that the CMAS penetration depth has a greater effect on the TC/TGO interface stress behavior, and might accelerate the initiation of crack at valleys of the CMAS penetrated side TC/TGO interface.

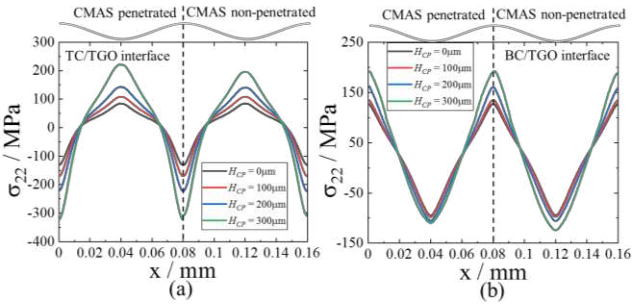

Figure 12 The σ_{22} distribution at (a) TC/TGO and (b) BC/TGO interface under different CMAS penetration depths

3.3 The effect of interface roughness

Figure 13(a) and (b) show the interface temperature distribution of zone II under different interface amplitude (A=5 μm, 10 μm, 20 μm). All the cases are calculated with CMAS penetration depth HCP=300μm. The interface temperature distribution is asymmetrical around the dividing line of left side, and this asymmetrical phenomenon becomes more obvious as the A increases. As the interface amplitude increases from 5 μm to 20 μm, the temperature at the peak (point 1) increases by 12K, while the temperature at the peak of the right side (point 5) only increases by 8K, as shown in Figure 13(c). This illustrates that CMAS penetration aggravates the influence of interface roughness on the temperature at the peaks of the interface. The temperature at the valleys shows different trend with A: the temperature at the valley of the left side of the interface decreases (point 2), while the temperature at the valley of the right side of the interface increases slightly (point 4), this is due to the heat conduction from the adjacent peaks with high temperature in TGO.

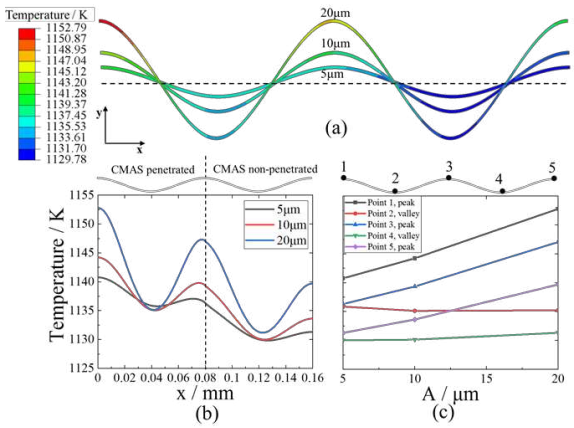

Figure 13 (a) The temperature contour of TGO in zone II under different interface amplitudes (*A*=5μm, 10μm, 20μm); (b) the interface temperature distribution of zone II under different interface amplitudes; (c) the temperature at the peaks and valleys of the interface under different interface amplitudes.

Figure 14(a) further exhibits distribution of TGO thickness with different interface amplitudes. Similar to the interface temperature distribution shown in Figure 13, the maximum TGO thickness appears at the peak of the left side (Point 1), while the minimum appears at the valley of the right side (Point 4). When the interface amplitude A increases from 5μm to 10μm, the TGO thickness increases slightly, while the TGO thickness increases sharply when A continues to increase up to 20 μm, as is shown in Figure 14(b). This demonstrates that TGO growth is not proportional to the interface amplitude.

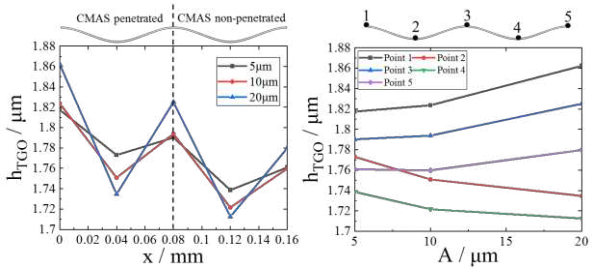

Figure 14 (a) The distribution of TGO thickness with different interface amplitudes; (b) TGO thickness at the peaks and valleys

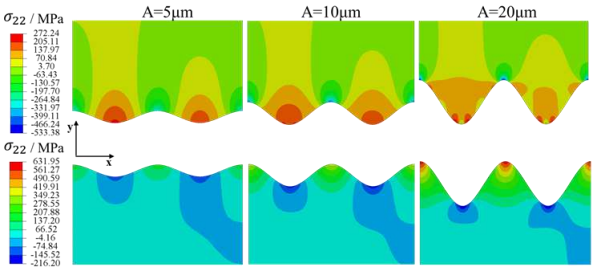

of the interface with different interface amplitudes.

Figure 15 The σ_{22} distribution in TC and BC layer of zone II under different interface amplitude

To investigate the effect of TGO thickness on the interface stress behavior in this model. Figure 15 shows the σ_{22} distribution in TC and BC layer of zone II under different interface amplitude. For the TC layer, the interface stress redistributes as the interface amplitude increases, and the maximum σ_{22} location gradually moves from the valley to the both side of it (off-valley). For the BC layer, as the when interface amplitude increases, the σ_{22} at the peaks increases sharply from 200 MPa to 630 MPa, while the maximum σ_{22} location shows no change. Figure 16 further the σ_{22} distribution at the TC/TGO and BC/TGO interface of zone II under different interface roughness. This figure clearly exhibits the stress redistribution at the TC/TGO interface, and the value of maximum σ_{22} increased slightly. The stress difference around the dividing line induced by the non-uniform CMAS penetration also increases slightly at the TC/TGO interface. Compared to the stress level at the TC/TGO interface, the maximum σ_{22} at the BC/TGO interface increases considerably, and the stress distribution shows some fluctuates when the interface amplitude increases to 20μm. To conclude, the interface roughness changes the stress distribution at the TC/TGO interface, but has a more obvious influence on the stress level at BC/TGO interface under CMAS penetration.

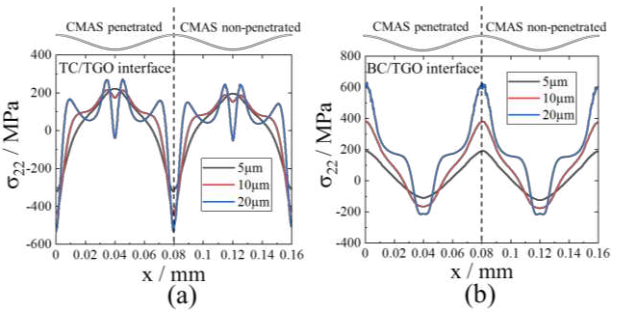

Figure 16 The σ_{22} distribution at the TC/TGO and BC/TGO interface of zone II under different interface roughness

4 Conclusions

This study numerically investigated the influence of CMAS penetration on the TGO growth and stress behavior at the TC/BC interface. Firstly, the change of thermal/mechanical properties induced by CMAS penetration is appropriately considered base on some theoretical models. The effect of non-uniform CMAS penetration is studied in a two-dimensional global model of APS TBCs with half of the TC penetrated by CMAS. The effects of interface roughness and CMAS penetration depth are also discussed based on a local model. The results indicated the following:

(1) CMAS penetration leads to the deterioration of the thermal insulation performance in the CMAS penetration area of APS TBCs, this further causes a temperature difference about 100 K between the penetrated and non-penetrated areas. The temperature gradients both exist in transverse direction and thickness direction;

(2) Non-uniform CMAS penetration in APS TBCs causes non-uniform TGO growth, which further leads to more complicated interface stress distribution. For the TC/TGO interface, CMAS penetration might accelerate the cracks initiation at the valleys; for the BC/TGO interface, CMAS penetration might accelerate cracks initiation at the peaks.

(3) When CMAS penetration depth increases, the difference of the interface tensile stress around the the dividing line of CMAS becomes larger. the

influence of CMAS penetration depth on the stress behavior at TC/TGO and BC/TGO interface is different. The CMAS penetration depth has a greater effect on the TC/TGO interface stress behavior, and might accelerate the initiation of crack at valleys of the CMAS penetrated side TC/TGO;

(4) Compared to the stress level at the TC/TGO interface, the maximum σ_{22} at the BC/TGO interface increases considerably. The interface roughness changes the stress distribution at the TC/TGO interface, but has an more obvious influence on the stress level at BC/TGO interface under CMAS penetration.

5 Declaration

Acknowledgements

The authors sincerely thanks to Professor Wang of Shanghai Jiao Tong University for his critical discussion and reading during manuscript preparation.

Funding

This project was supported by the National Natural Science Foundation of China (Grant No. 51875341).

Availability of data and materials

The datasets supporting the conclusions of this article are included within the article.

Authors' contributions

Cai and Wang conceived and designed the study. Cai and Zhang performed the numerical calculations. Liu and Zhao provided the experimental figures. Cai wrote the initial draft of the paper. Liu, Zhao and Wang reviewed and edited the manuscript. All authors read and approved the manuscript.

Competing interests

We declare that we do not have any commercial or associative interest that represents a conflict of interest in connection with the work submitted.

Consent for publication

Not applicable

Ethics approval and consent to participate

Not applicable

References

[1] Schlichting K W, Padture N P, Jordan E H, et al. Failure modes in plasma-sprayed thermal barrier coatings. Materials Science & Engineering A (Structural Materials: Properties, Microstructure and Processing), 2003, 342(1-2):120-130.

[2] Chen W R, Zhao L R. Review: Volcanic ash and its influence on aircraft engine components. Procedia Engineering, 2015, 99:795-803.

[3] Cai Z, Jiang J, Wang, et al. CMAS penetration-induced cracking behavior in the ceramic top coat of APS TBCs[J]. Ceramics International, 2019, 45(11).

[4] Cai Z, Hong H, Peng D, et al. Stress evolution in ceramic top coat of air plasma-sprayed thermal barrier coatings due to CMAS penetration under thermal cycle loading[J]. Surface and Coatings Technology, 2019, 381:125146.

[5] Krämer S, Faulhaber S, Chambers M, et al. Mechanisms of cracking and delamination within thick thermal barrier systems in aero-engines subject to calcium-magnesium-alumino-silicate (CMAS) penetration. Materials Science & Engineering A, 2008, 490(1):26-35.

[6] Krause A R, Garces H F, Dwivedi G, et al. Calcia-magnesia-alumino-silicate (CMAS)-induced degradation and failure of air plasma sprayed yttria-stabilized zirconia thermal barrier coatings. Acta Materialia, 2016, 105:355-366.

[7] Lokachari S, Song W, Yuan J, et al. Influence of molten volcanic ash infiltration on the friability of APS thermal barrier coatings[J]. Ceramics International, 2020, 46(8).

[8] Kakuda T R, Levi C G, Bennett T D. The thermal behavior of CMAS-infiltrated thermal barrier coatings. Surface and Coatings Technology, 2015, 272:350-356.

[9] Darolia, R. Thermal barrier coatings technology: critical review, progress update, remaining challenges and prospects[J]. International Materials Reviews, 2013, 58(6):315-348.

[10] Wu Y, Luo H, Cai C, et al. Comparison of CMAS corrosion and sintering induced microstructural characteristics of APS thermal barrier coatings[J]. Journal of Materials Science & Technology, 2019, 35(3): 440-447.

[11] Nakamura T, Wang T, Sampath S. Determination of properties of graded materials by inverse analysis and instrumented indentation[J]. Acta Materialia, 2000, 48(17):4293-4306.

[12] Su L, Wang T J, *et al*. Numerical analysis of CMAS penetration induced interfacial delamination of transversely isotropic ceramic coat in thermal barrier coating system[J]. Surface & Coatings Technology, 2015.

[13] Su L, Yi C. Effects of CMAS penetration on the delamination cracks in EB-PVD thermal barrier coatings with curved interface[J]. Ceramics International, 2017:8893-8897.

[14] Maxwell J C A. A Treatise on Electricity and Magnetism[J]. Nature, 7(182):478-480.

[15] Rayleigh, Lord. LVI. On the influence of obstacles arranged in rectangular order upon the properties of a medium[J]. Philosophical Magazine, 1892, 34(211):481-502.

[16] Zhang G, Fan X, Xu R, et al. Transient thermal stress due to the penetration of calcium-magnesium-alumino-silicate in EB-PVD thermal barrier coating system[J]. Ceramics International, 2018: S0272884218309362.

[17] Yuan K, Yu Y, Wen J F. A study on the thermal cyclic behavior of thermal barrier coatings with different MCrAlY roughness[J]. Vacuum, 2017, 137:72-80.

[18] Yu Q M, Zhou H L, Wang L B. Influences of interface morphology and thermally grown oxide thickness on residual stress distribution in thermal barrier coating system[J]. Ceramics International, 2016,

42(7):8338-8350.

[19] Si K, Jones A, Jepson M A E, et al. Effects of three-dimensional coating interfaces on thermo-mechanical stresses within plasma spray thermal barrier coatings[J]. Materials & Design, 2017, 125:189-204.

[20] Mack D E, Wobst T, Jarligo M O D, et al. Lifetime and failure modes of plasma sprayed thermal barrier coatings in thermal gradient rig tests with simultaneous CMAS injection. Surface and Coatings Technology, 2017: S0257897217304474.

[21] Jackson R W., Zaleski E M., Poerschke D L, et al. Interaction of molten silicates with thermal barrier coatings under temperature gradients[J]. Acta Materialia, 2015, 89: 396-407.

[22] Chiang Y M, Birnie D P, Kingery W D. Physical ceramics[J]. 1997.

[23] Hashin Z. On elastic behaviour of fibre reinforced materials of arbitrary transverse phase geometry[J]. Journal of the Mechanics & Physics of Solids, 1965, 13(3):119-134.

[24] Wu J, Guo H B, Gao Y Z, et al. Microstructure and thermo-physical properties of yttria stabilized zirconia coatings with CMAS deposits[J]. Journal of the European Ceramic Society, 2011, 31(10):1881-1888.

[25] Schapery R A, et al. Thermal Expansion Coefficients of Composite Materials Based on Energy Principles[J]. Journal of Composite Materials, 1968, 2.

[26] Kumar R, Cietek D, Jiang C, et al. Influence of microstructure on the durability of gadolinium zirconate thermal barrier coatings using APS & SPPS processes[J]. Surface and Coatings Technology, 2018, 337:117-125.

[27] Cai L, Ma W, Ma B, et al. Air Plasma-Sprayed La2Zr2O7-SrZrO3 Composite Thermal Barrier Coating Subjected to CaO-MgO-Al_2O_3-SiO_2 (CMAS)[J]. Journal of Thermal Spray Technology, 2017, 26(5566):1-8.

[28] Wang Z, Kulkarni A, Deshpande S, et al. Effects of pores and

[29] Kulkarni A, Wang Z, Nakamura T, et al. Comprehensive microstructural characterization and predictive property modeling of plasma-sprayed zirconia coatings[J]. Acta Materialia, 2003, 51(9):2457-2475

[30] Kulkarni A, Wang Z, Nakamura T, et al. Comprehensive microstructural characterization and predictive property modeling of plasma-sprayed zirconia coatings[J]. Acta Materialia, 2003, 51(9):2457-2475.

[31] Schulz U, Leyens C, Fritscher K, et al. Some Recent Trends in Research and Technology of Advanced Thermal Barrier Coatings[J]. Aerospace ence and Technology, 2003, 7(1):73-80.

[32] Wang W, Sun P, Ren J, et al. Radiative Effectiveness on the Aero and Thermodynamics in a Highly Thermally Loaded Film Cooling System[C]. ASME 2011 Turbo Expo: Turbine Technical Conference and Exposition. 2011:325-334.

[33] Version ABAQUS. 6.13, Analysis user's guide. Dassault Systems, 2013.

[34] Su L, Zhang W, Sun Y, et al. Effect of TGO creep on top-coat cracking induced by cyclic displacement instability in a thermal barrier coating system[J]. Surface & Coatings Technology, 2014, 254:410-417.

[35] Ranjbar-Far M, Absi J, Shahidi S, et al. Impact of the non-homogenous temperature distribution and the coatings process modeling on the thermal barrier coatings system[J]. Materials & Design, 2011, 32(2):728-735.

[36] Kim K M, Shin S, Dong H L, et al. Influence of material properties on temperature and thermal stress of thermal barrier coating near a normal cooling hole[J]. International Journal of Heat & Mass Transfer, 2011, 54(25–26):5192-5199.

[37] Wang L, Wang Y, Sun X G, et al. Influence of pores on the thermal insulation behavior of thermal barrier coatings prepared by atmospheric plasma spray[J]. Materials & Design, 2011, 32(1):36-47.

[38] Zaretsky E B, Kanel G I, Razorenov S V, et al. Impact strength properties of nickel-based refractory superalloys at normal and elevated temperatures[J]. International Journal of Impact Engineering, 2005, 31(1):41-54.

[39] Hyde C J, Hyde T H, Sun W, et al. Small ring testing of a creep resistant material[J]. Materials Science & Engineering A Structural Materials Properties Microstructure & Processing, 2013, 586(6):358-366.

[40] Jiang J, Wang W, Zhao X, et al. Numerical analyses of the residual stress and top coat cracking behavior in thermal barrier coatings under cyclic thermal loading. Engineering Fracture Mechanics, 2018, 196:191-205.

[41] Wiesner V L, Bansal N P. Mechanical and thermal properties of calcium–magnesium aluminosilicate (CMAS) glass[J]. Journal of the European Ceramic Society, 2015, 35(10):2907-2914.

[42] Beck T, Herzog R, Trunova O, et al. Damage mechanisms and lifetime behavior of plasma-sprayed thermal barrier coating systems for gas turbines — Part II: Modeling[J]. Surface & Coatings Technology, 2008, 202(24):5901-5908.

Biographical notes

Zhen-Wei Cai, born in 1992, is a postdoctor at *Key Laboratory of Power Machinery and Engineering, School of Mechanical Engineering, Shanghai Jiao Tong University, Shanghai 200240, China*. His main research direction is the strength evaluation of high-temperature structural components and the intelligent manufacturing of advanced thermal barrier coatings
Tel: +86-18801733509; E-mail: xiaoyezhu1992@sjtu.edu.cn

Zi-Fan Zhang, born in 1996, is currently a master student at *Key Laboratory of Power Machinery and Engineering, School of Mechanical Engineering, Shanghai Jiao Tong University*. His main research direction is the strength evaluation of thermal barrier coatings.
E-mail: 954143356@sjtu.edu.cn

Ying-Zheng Liu, born in 1972, is currently a professor at *Key Laboratory of Power Machinery and Engineering, School of Mechanical Engineering, Shanghai Jiao Tong University, Shanghai 200240, China.* He is the director of *Gas Turbine Research Institute, Shanghai Jiao Tong University, Shanghai 200240, China*
E-mail: yzliu@sjtu.edu.cn

Xiao-Feng Zhao, is currently a professor at *School of Materials Science and Engineering, Shanghai Jiao Tong University, Shanghai 200240, China.* His main research direction is high-temperature coatings, such as thermal barrier coatings used in aero engines and gas turbines, anti-corrosion coatings for nuclear reactor fuel claddings, and other anti-oxidation and wear-resistant coatings.
E-mail: xiaofengzhao@sjtu.edu.cn

Wei-Zhe Wang, born in 1977, is currently a professor at *Gas*

Turbine Research Institute, Shanghai Jiao Tong University, Shanghai 200240, China. He mainly focuses on the major national demand industries (aviation, ground gas turbines, smart energy), and conducts research on digital twin technology of process systems and component systems.
Tel: +86- 021-34205083; E-mail: wangwz0214@sjtu.edu.cn

Appendix

Not applicable

Figures

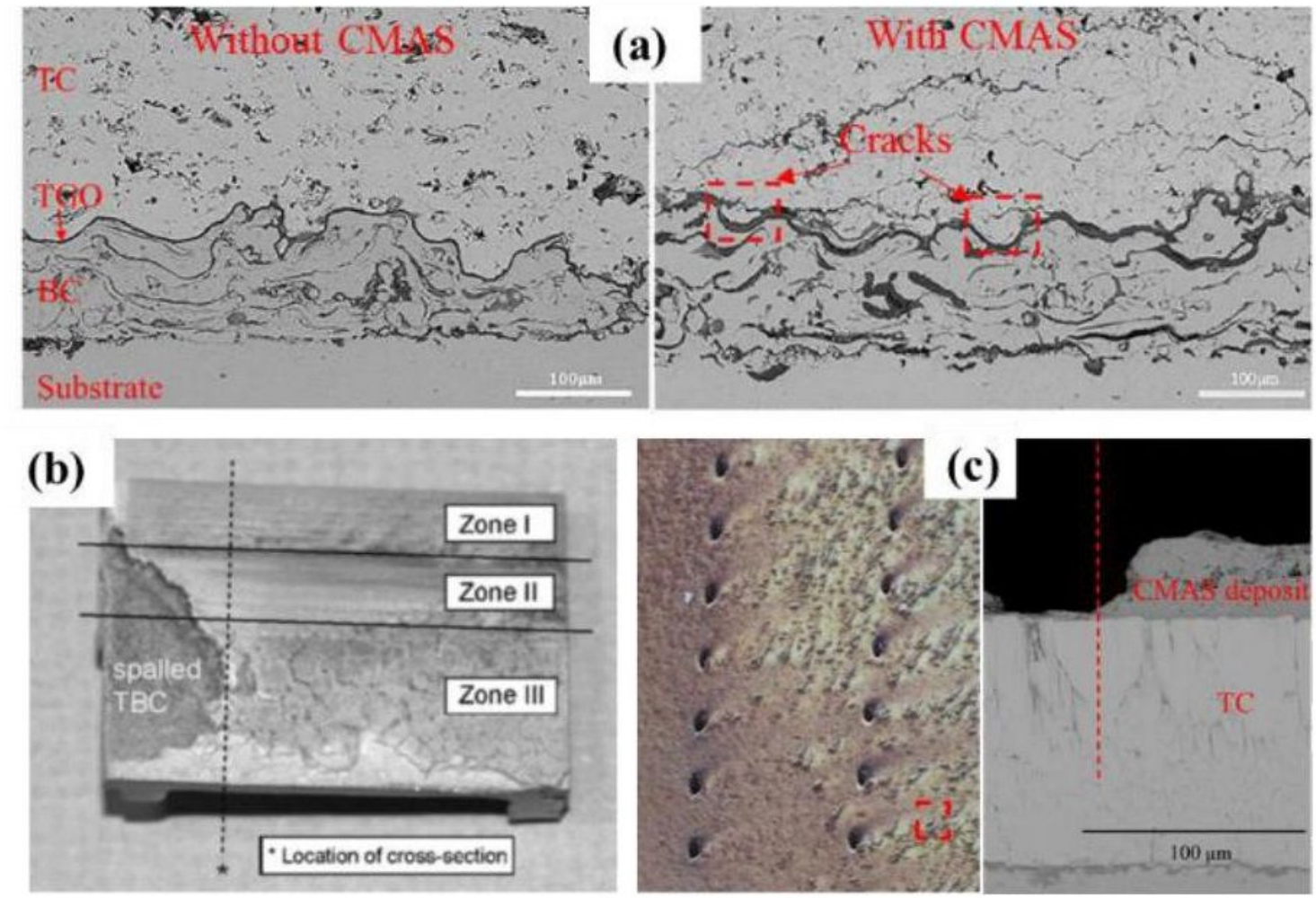

Figure 1

(a) Cross-section of APS TBCs without/with CMAS penetration; (b) Cross-section image of the uniform CMAS deposit distribution around the dividing line; (c) Plan view optical image of a segment of a turbine shroud.

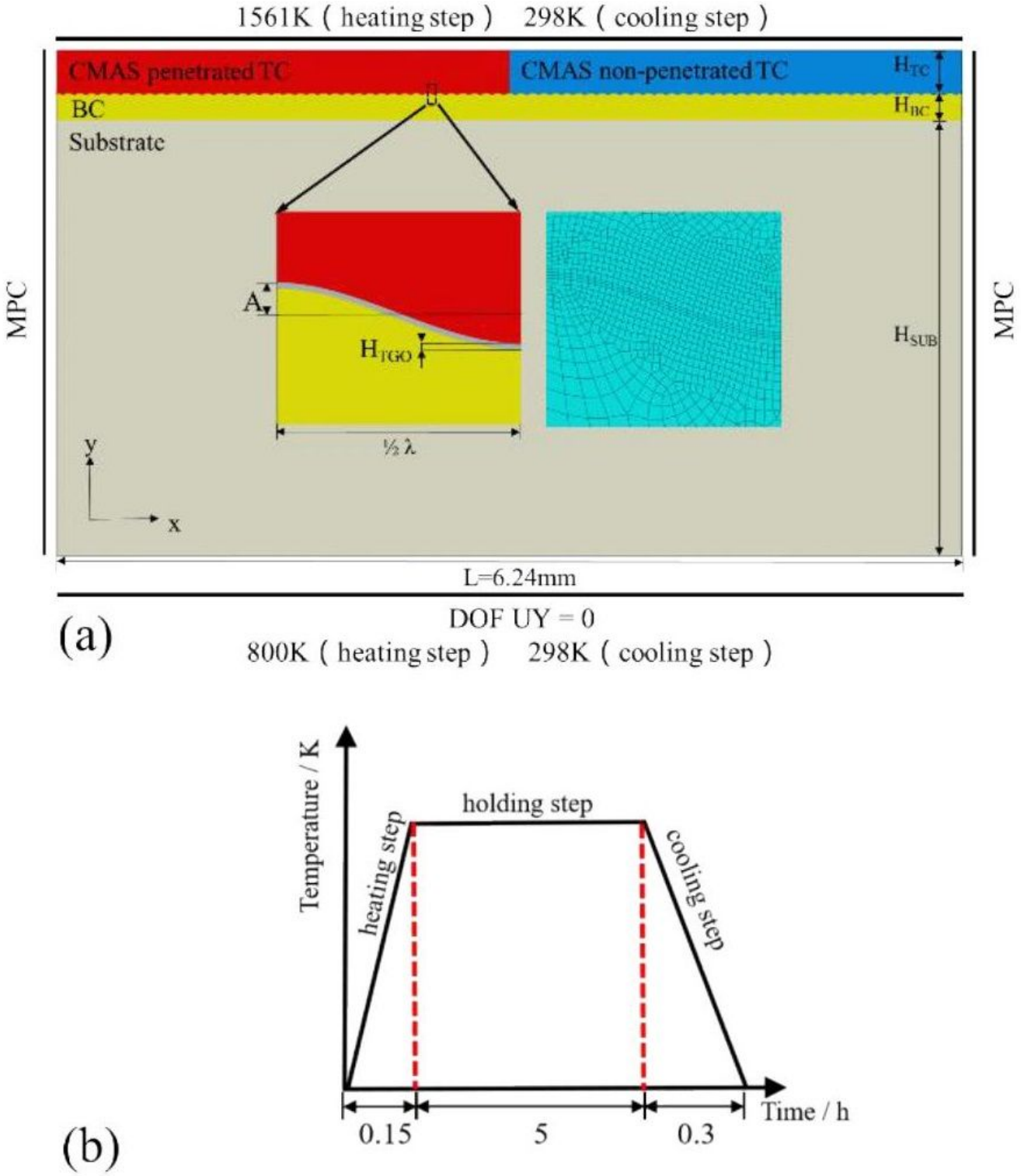

Figure 2

(a) The two-dimensional multi-period global model of APS TBCs with CMAS non-uniform penetration; (B) Thermal boundary conditions of the model.

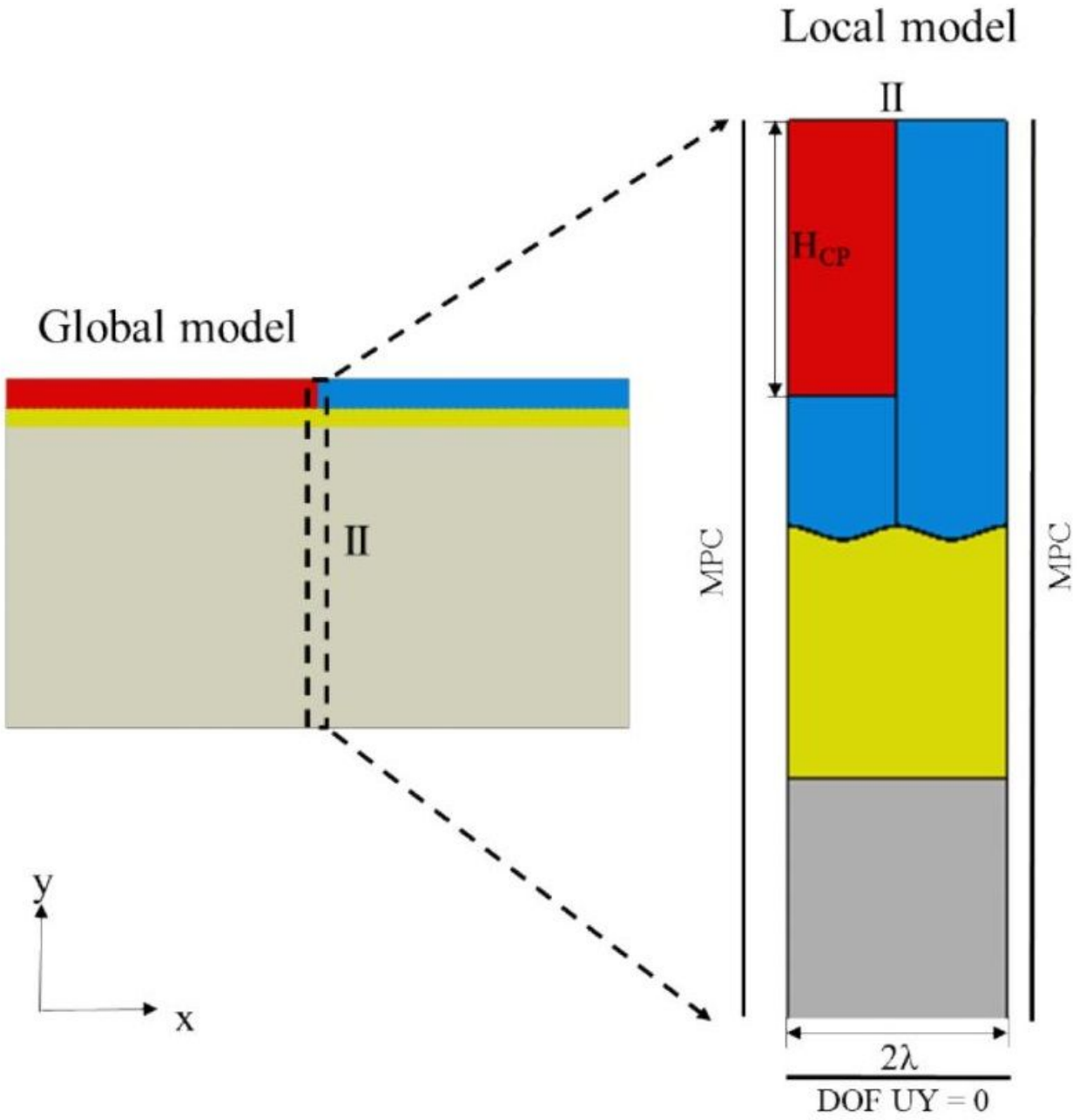

Figure 3

The local model of the critical zone II.

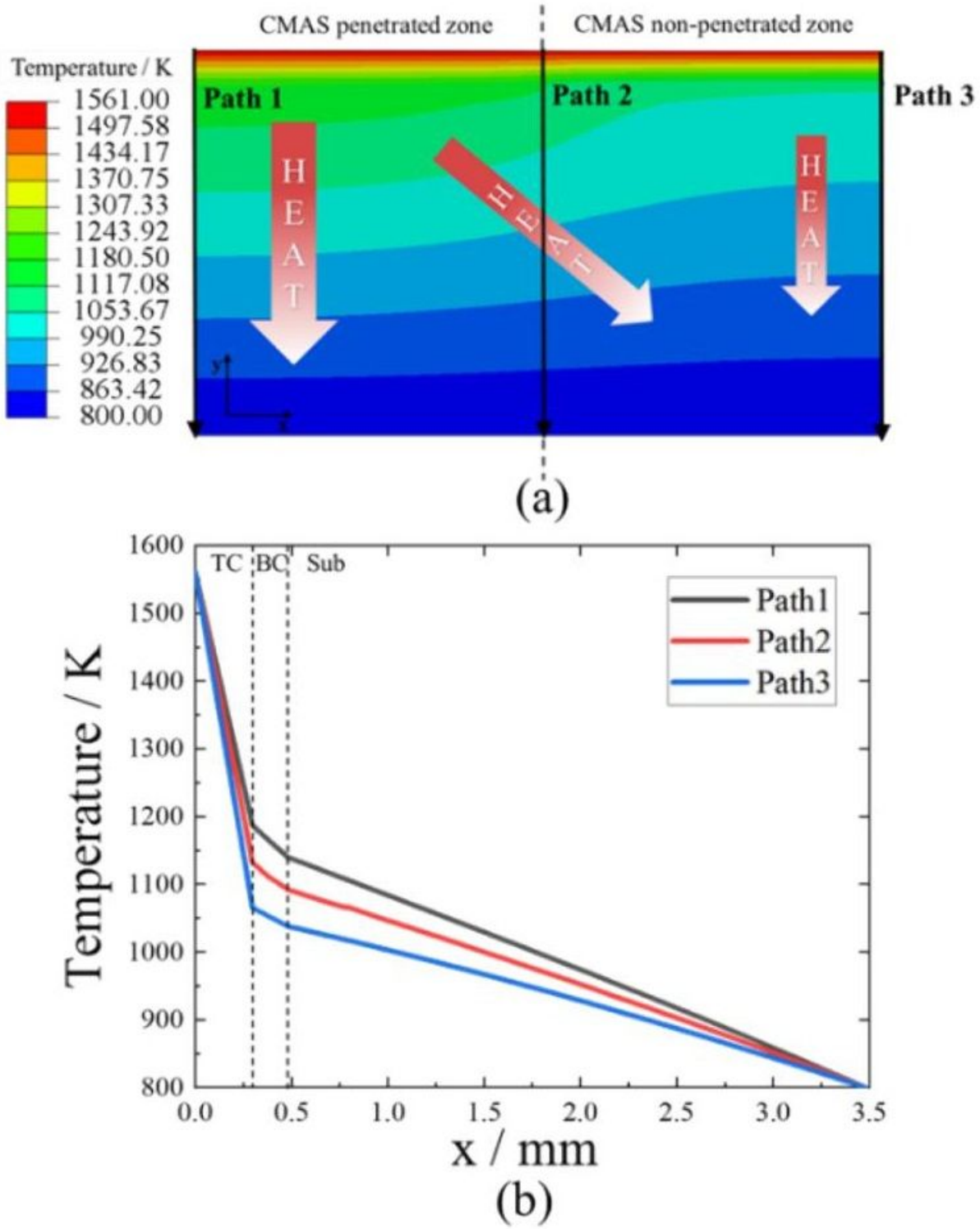

Figure 4

(a) The temperature distribution of the multi-period global model of APS TBCs under the non-uniform CMAS penetration; (b) The temperature distributions along THEthree paths in the model.

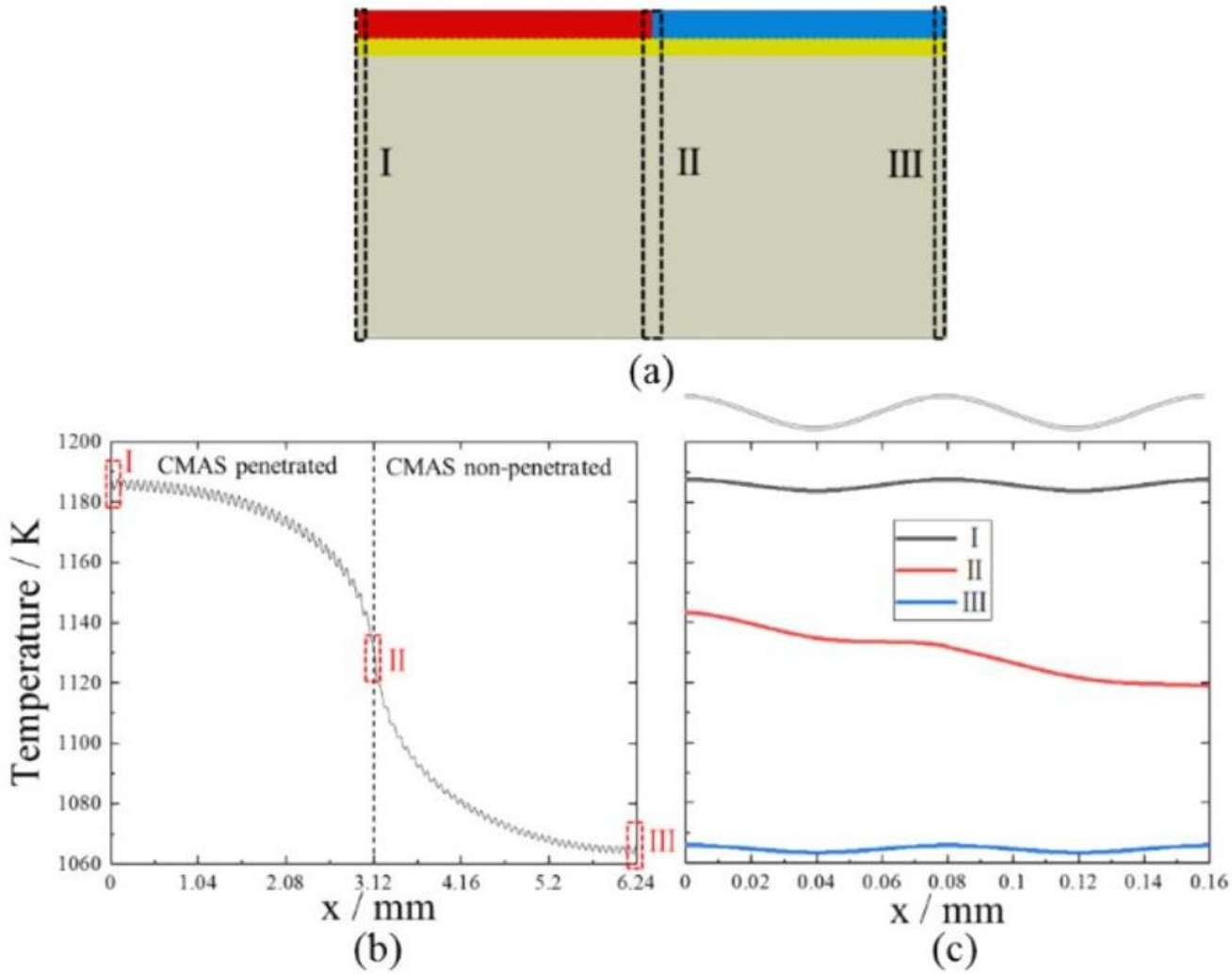

Figure 5

(a) The critical zones: I, II and III; (b) the temperature distribution at the interface of the multi-period model after the heating process; (c) the interface temperature distribution in three critical zones: I, II, and III.

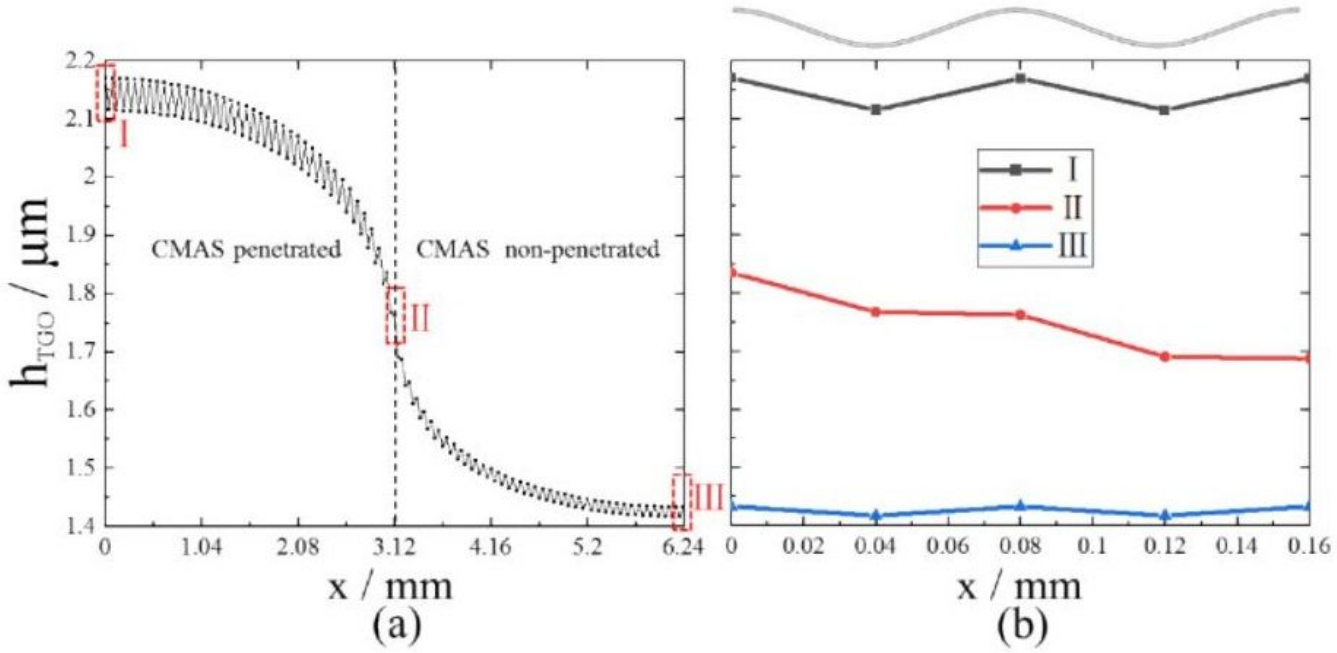

Figure 6

(a)The distribution of TGO thickness in the multi-period global model of APS TBCs; (b) The distribution of TGO thickness in three critical zones: I, II, and III

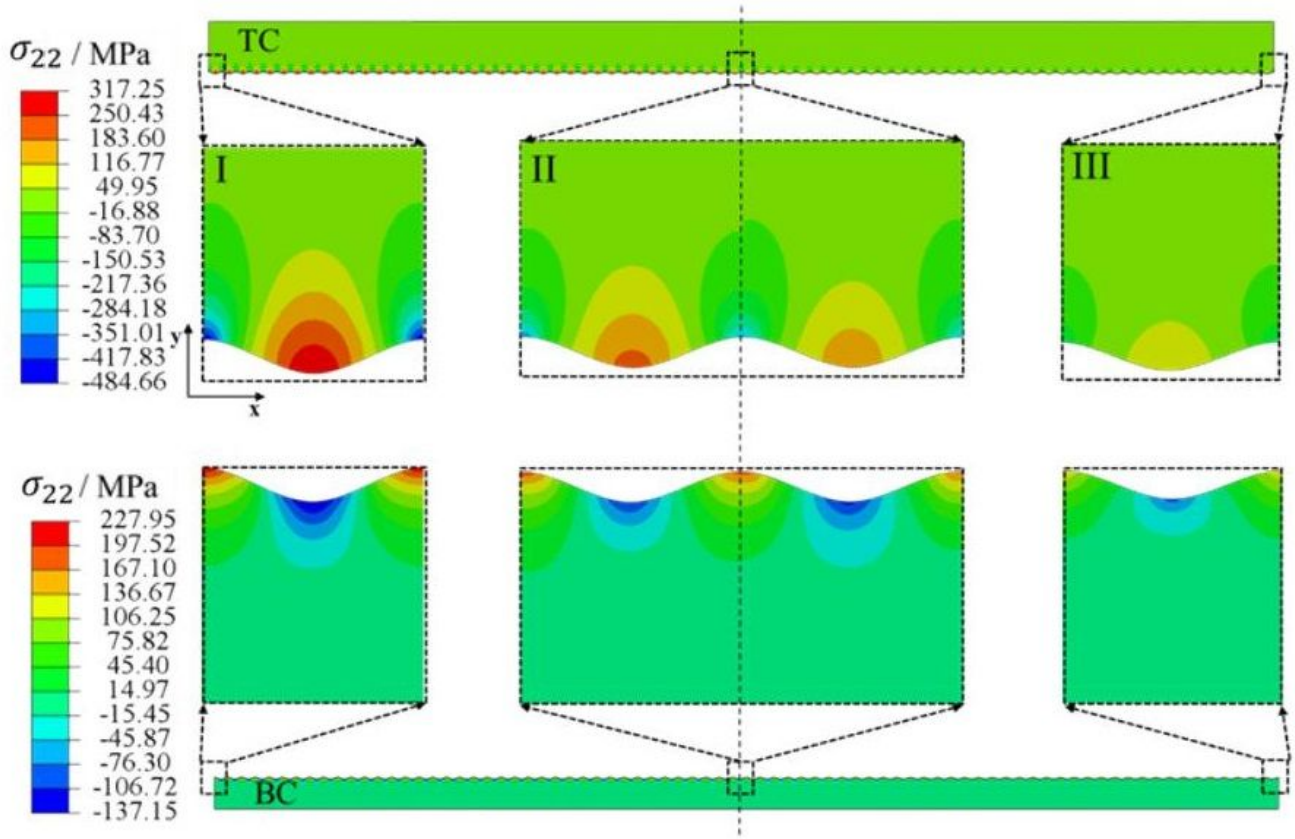

Figure 7

The σ22 distribution in TC and BC layer of the multi-period global model of APS TBCs at room temperature

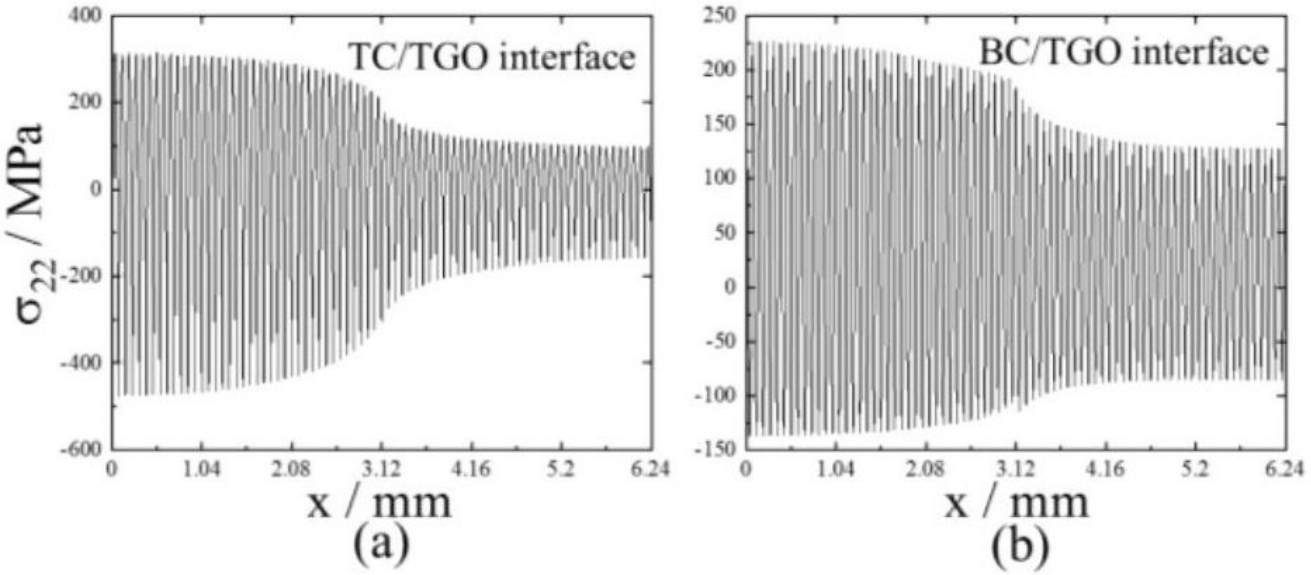

Figure 8

The σ22 distribution at (a) TC/TGO and (b) BC/TGO interface of the multi-period global model of APS TBCs

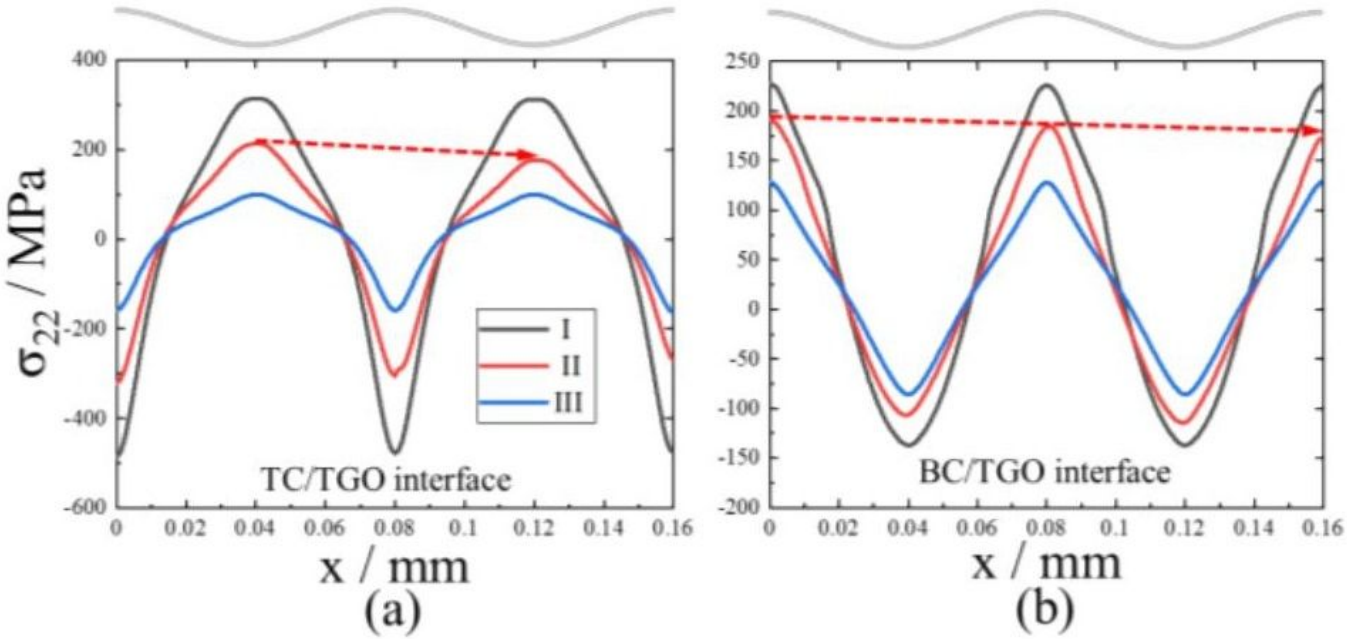

Figure 9

The σ22 distribution at (a) TC/TGO and (b) BC/TGO of the three critical zones.

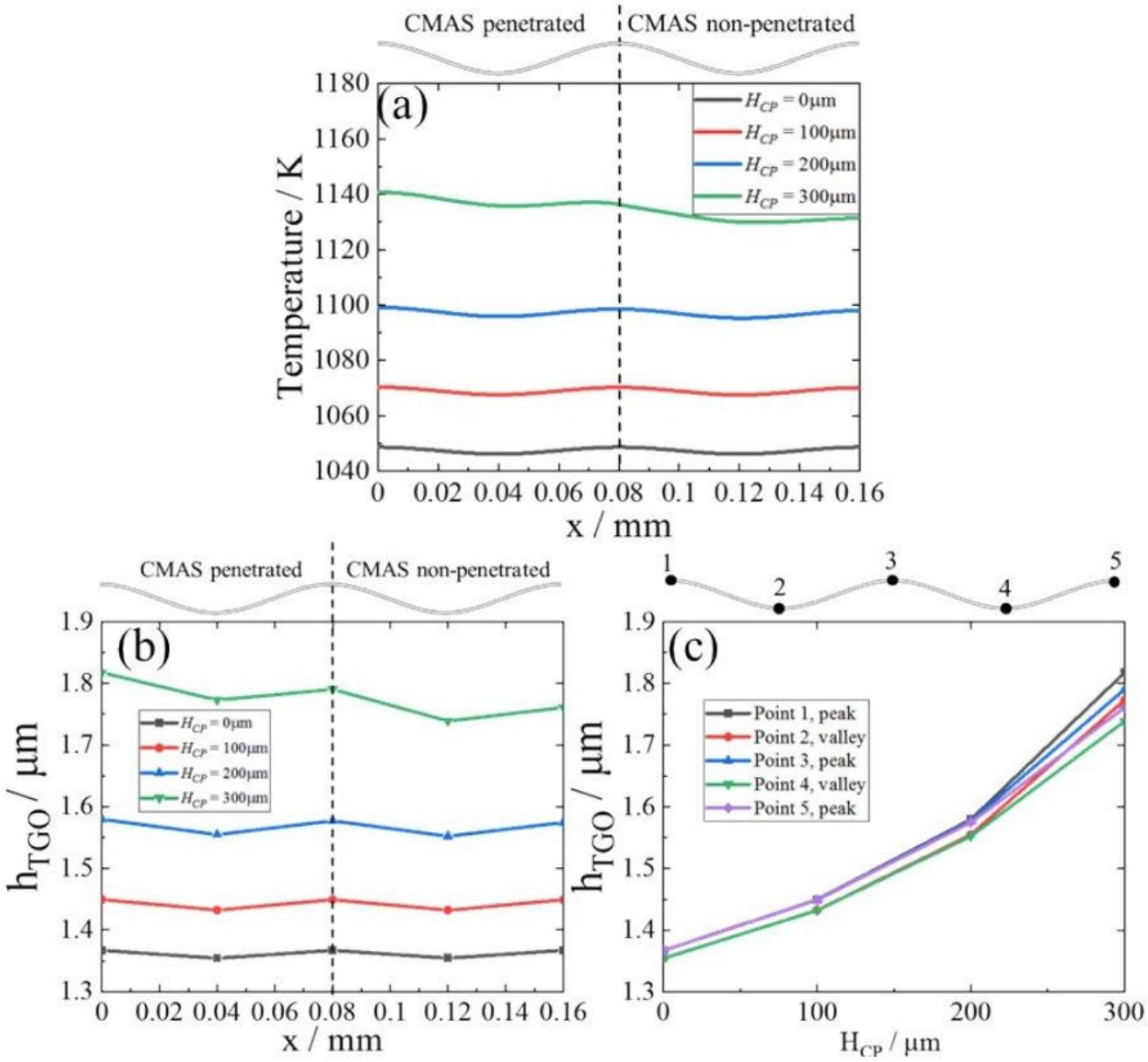

Figure 10

(a) The temperature distribution at the interface of zone II under different CMAS penetration depths (HCP=0μm, 100μm, 200μm, 300μm); (b) the distribution of TGO thickness under different CMAS penetration depths; (c) TGO thickness at the peaks and valleys of the interface under different CMAS penetration depth

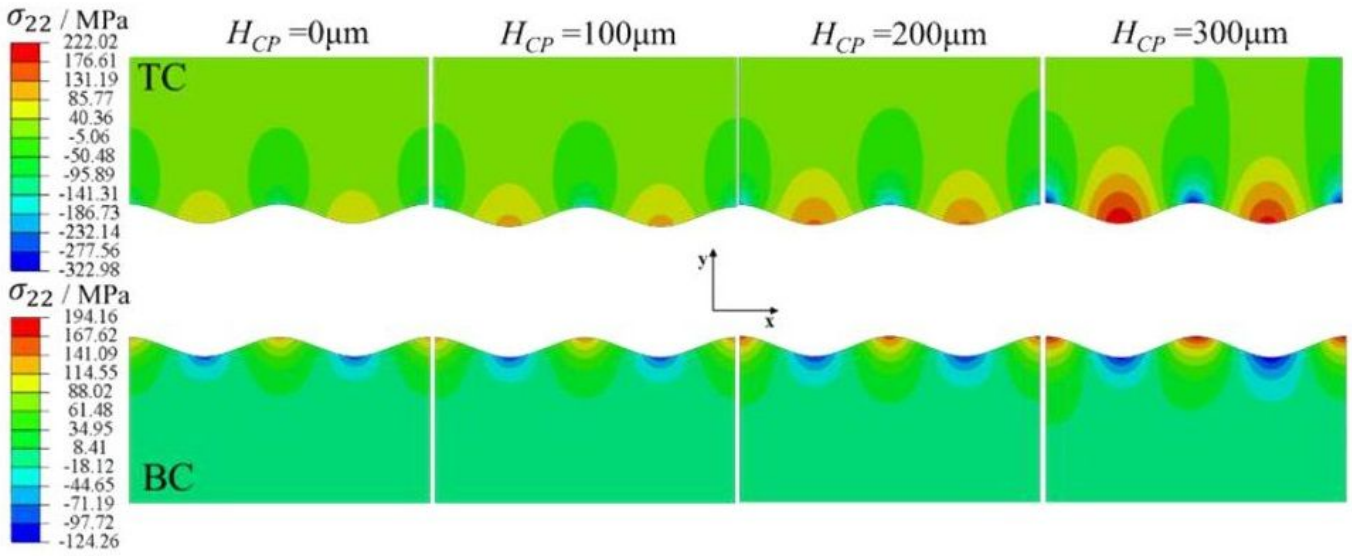

Figure 11

The σ22 distribution in TC and BC layer of zone II under different CMAS penetration depths.

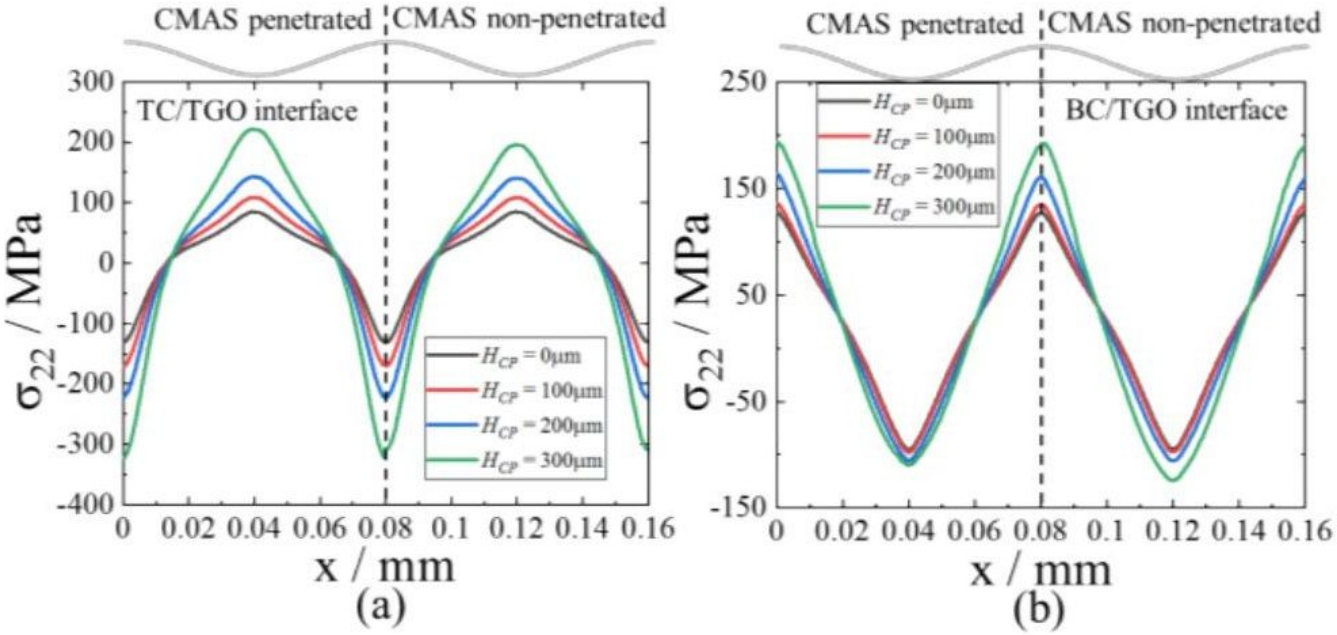

Figure 12

The σ22 distribution at (a) TC/TGO and (b) BC/TGO interface under different CMAS penetration depths

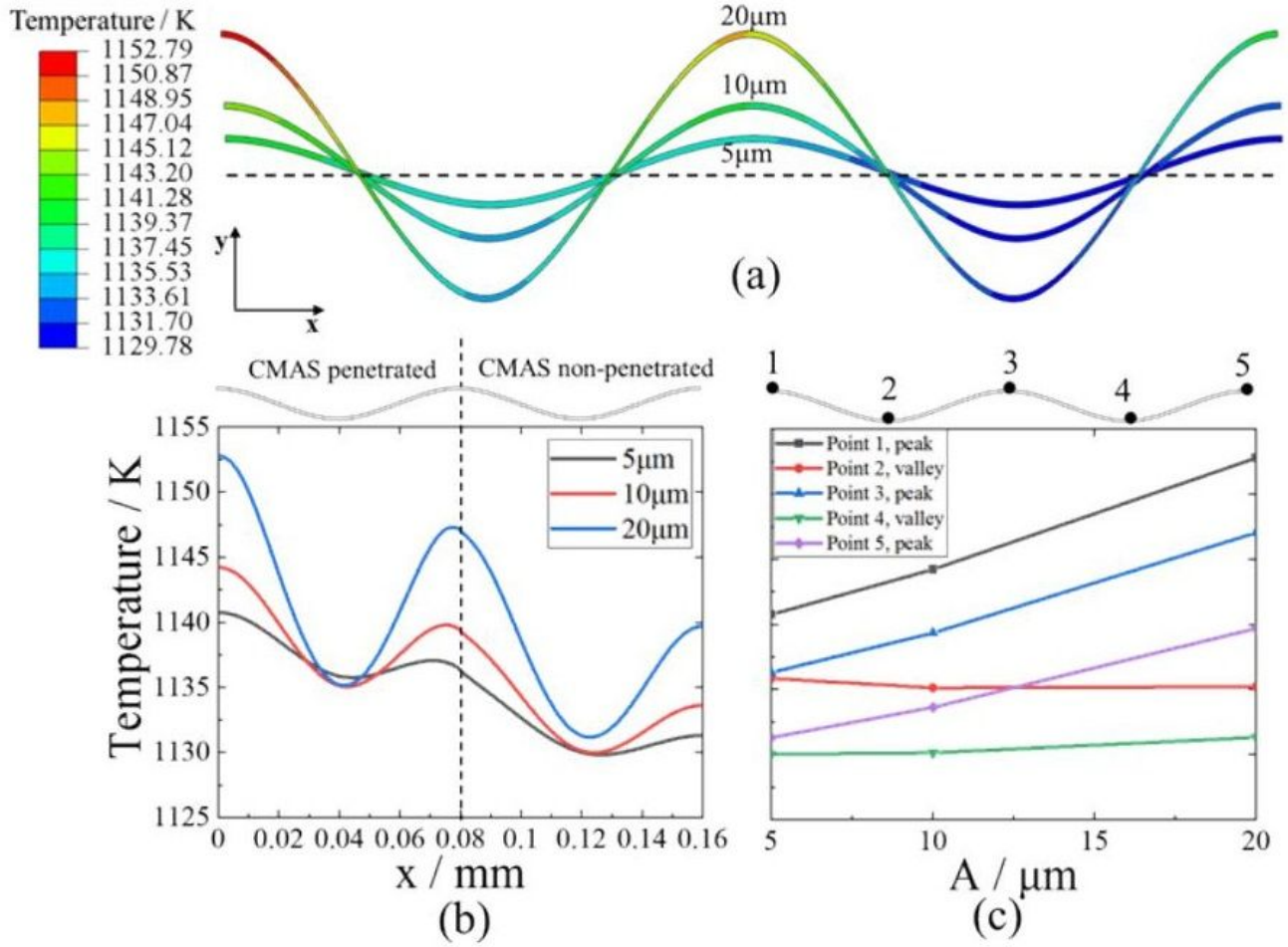

Figure 13

(a) The temperature contour of TGO in zone II under different interface amplitudes (A=5μm, 10μm, 20μm); (b) the interface temperature distribution of zone II under different interface amplitudes; (c) the temperature at the peaks and valleys of the interface under different interface amplitudes.

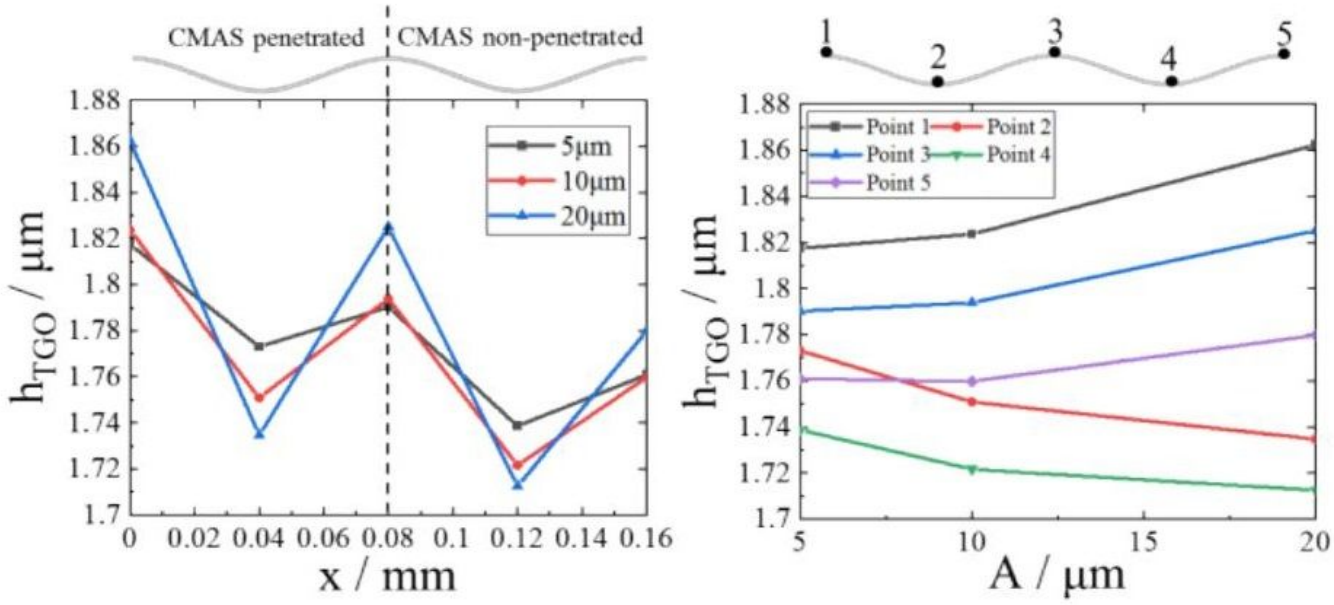

Figure 14

(a) The distribution of TGO thickness with different interface amplitudes; (b) TGO thickness at the peaks and valleys of the interface with different interface amplitudes.

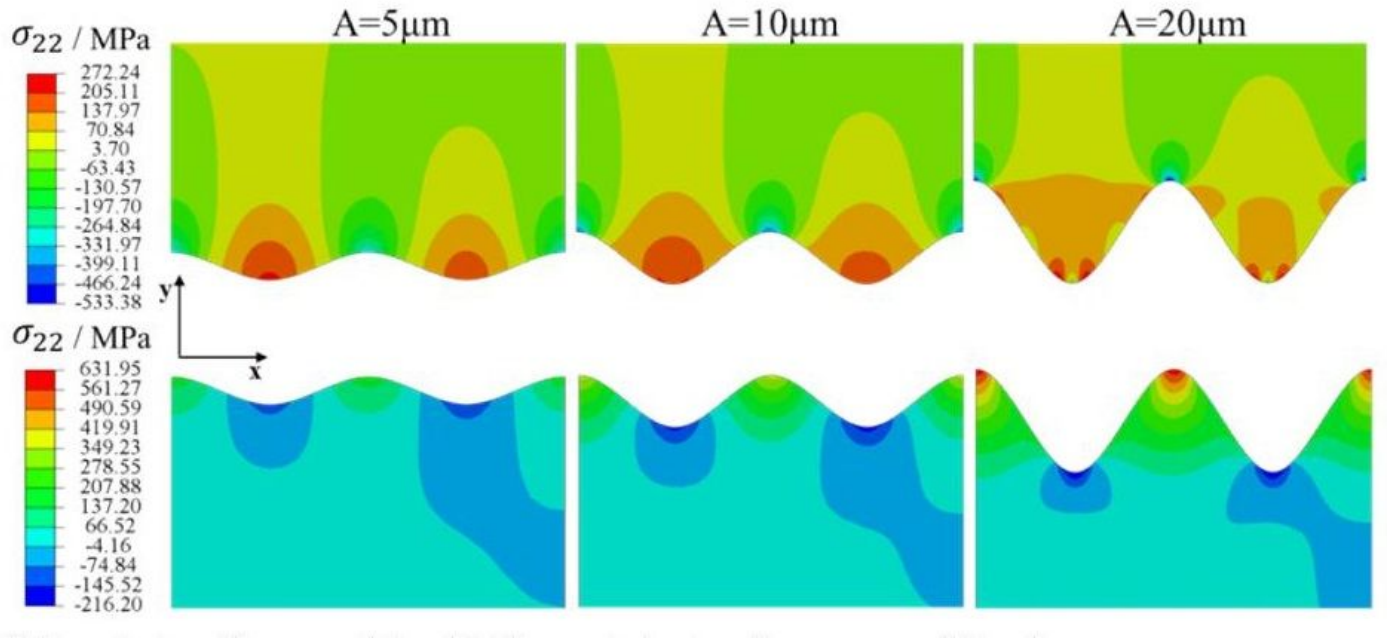

Figure 15

The σ22 distribution in TC and BC layer of zone II under different interface amplitude

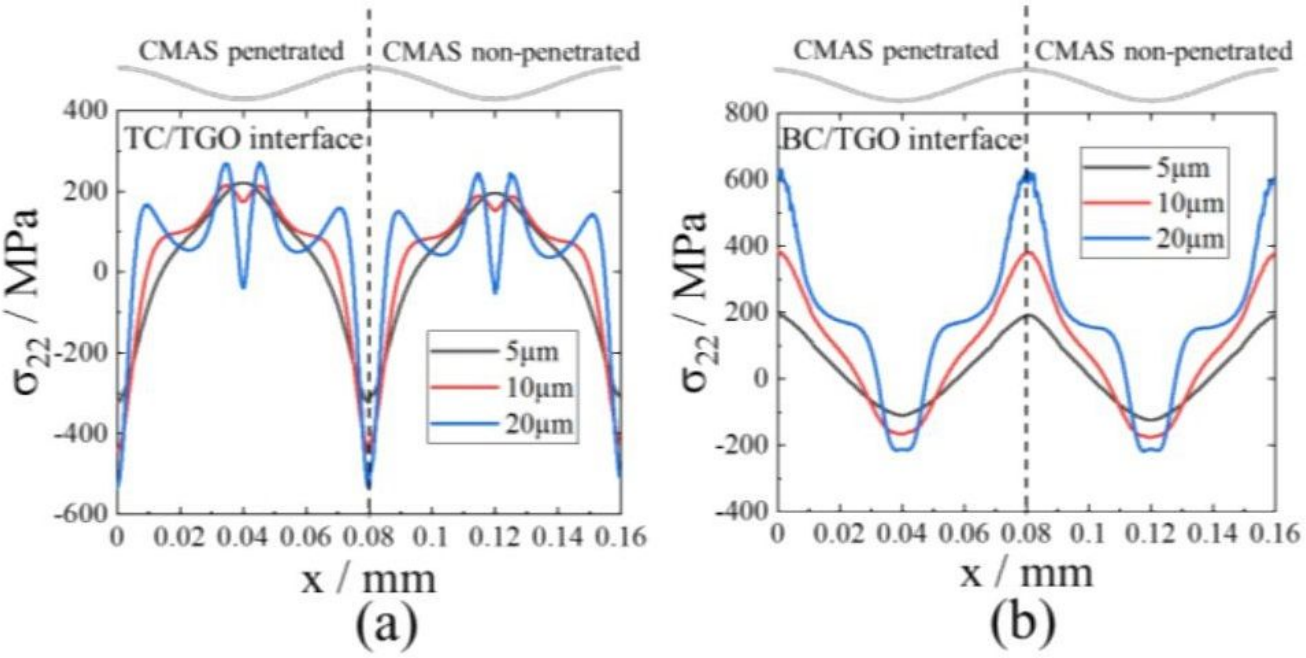

Figure 16

The σ22 distribution at the TC/TGO and BC/TGO interface of zone II under different interface roughness